Research Square

Preprints are preliminary reports that have not undergone peer review.
They should not be considered conclusive, used to inform clinical practice,
or referenced by the media as validated information.

Multi-omics reveals the DR5-FXR-CHPT1 axis governs hepatocyte pyroptosis via glycerophospholipid remodeling after major partial hepatectomy

Hua Li

lihua3@mail.sysu.edu.cn

The Third Affiliated Hospital of Sun Yat-sen University

Yongsheng tang

The Third Affiliated Hospital of Sun Yat-sen University

XU LU

the Third Affiliated Hospital of Sun Yat-sen University

Xi Luo

the Third Affiliated Hospital of Sun Yat-sen University

Qinghai Lian

The Third Affifiliated Hospital, Sun Yat-sen University

Yingqiu Song

the Third Affiliated Hospital of Sun Yat-sen University

Manqiu Kang

the Third Affiliated Hospital of Sun Yat-sen University

Zihan Qiao

the Third Affiliated Hospital of Sun Yat-Sen University

Zhihua Rao

the Third Affiliated Hospital of Sun Yat-sen University

Linsen Ye

The Third Affiliated Hospital of Sun Yat-sen University https://orcid.org/0000-0001-9632-1949

Zenan Yuan

Third Affiliated Hospital of Sun Yat-sen University

Changchang JIA

The Third Affiliated Hospital of Sun Yat-Sen University https://orcid.org/0000-0002-5243-0008

Article

Keywords: Partial hepatectomy (PHx), Pyroptosis, Post-hepatectomy liver failure (PHLF), Small-for-size syndrome (SFSS), Glycerophospholipid metabolism, Death receptor 5 (DR5), Endoplasmic reticulum stress (ERS)

Posted Date: March 20th, 2026

DOI: https://doi.org/10.21203/rs.3.rs-9039762/v1

License: This work is licensed under a Creative Commons Attribution 4.0 International License. Read Full License

Additional Declarations: There is **NO** Competing Interest.

Version of Record: A version of this preprint was published at Nature Communications on October 7th, 2026. See the published version at https://doi.org/10.1038/s41467-026-78113-8.

Multi-omics reveals the DR5-FXR-CHPT1 axis governs hepatocyte pyroptosis via glycerophospholipid remodeling after major partial hepatectomy

Yongsheng Tang[1*], Xu Lu[1*], Xi Luo[1*], Qinghai Lian[2*], Yingqiu Song[3], Manqiu Kang[2], Zihan Qiao[2], Zhihua Rao[4], Linsen Ye[1#], Zenan Yuan[1#], Changchang Jia[2#], Hua Li[1#]

1.Department of Hepatic Surgery, Liver Transplantation Center, the Third Affiliated Hospital of Sun Yat-sen University, Guangzhou 510630, China
2.Department of Cell-Gene Therapy Translational Medicine Research Center, the Third Affiliated Hospital of Sun Yat-Sen University, Guangzhou 510630, China
3.Department of Hepatobiliary and Pancreatic Surgery, Zhuhai Branch, Guangdong Provincial Hospital of Traditional Chinese Medicine, Zhuhai, 19000, China
4.Department of Experimental Medicine, the Third Affiliated Hospital of Sun Yat-sen University, Guangzhou 510630, China

[*]These authors have contributed equally to this work.

[#]Corresponding author: Linsen Ye, ye_linsen@163.com; Zenan Yuan, yuanzn5@mail.sysu.edu.cn; Changchang Jia, jiachch3@mail.sysu.edu.cn; Hua Li, lihua3@mail.sysu.edu.cn.

Keywords: Partial hepatectomy (PHx); Pyroptosis; Post-hepatectomy liver failure (PHLF); Small-for-size syndrome (SFSS); Glycerophospholipid metabolism; Death receptor 5 (DR5); Endoplasmic reticulum stress (ERS).

Abstract

Acute liver injury following major partial hepatectomy (PHx), manifesting as small-for-size syndrome (SFSS) and post-hepatectomy liver failure (PHLF), carries high mortality. However, the key mechanisms underlying irreversible remnant liver injury and cell death remain poorly understood, particularly regarding the contribution of lipid metabolism. To address this, the current study investigates the role of lipid metabolism remodeling in post-hepatectomy hepatocyte injury to identify potential therapeutic targets. By integrating murine graded PHx models and human liver tissues from associating liver partition and portal vein ligation for staged hepatectomy (ALPPS) procedures with multi-omics and machine learning, we identified key regulatory genes. The underlying mechanisms were then validated via in vitro and in vivo genetic manipulation, alongside pharmacological modulation. Our findings reveal that aberrant glycerophospholipid metabolism is the primary driver of endoplasmic reticulum stress (ERS)-mediated pyroptosis in the remnant liver. Specifically, multi-omics analysis combined with machine learning identified death receptor 5 (DR5) as a critical regulator of this process. Mechanistically, DR5 physically impedes the nuclear translocation of the Farnesoid X Receptor (FXR), thereby repressing the transcription of *Chpt1* (Cholinephosphotransferase 1). The consequent deficiency in phosphatidylcholine (PC) compromises ER membrane integrity, exacerbating the Unfolded Protein Response and triggering lethal pyroptosis. Strikingly, restoring the DR5-FXR-CHPT1 axis via AAV-mediated DR5 knockdown, FXR agonists, or exogenous PC supplementation significantly alleviated

post-hepatectomy liver injury. Ultimately, this study uncovers a non-canonical metabolic function of DR5 that disrupts ER membrane homeostasis via the FXR-CHPT1 axis, leading to fatal hepatocyte pyroptosis. Targeting this active metabolic reprogramming offers a promising therapeutic strategy to prevent PHLF and SFSS after major PHx.

Introduction

Partial hepatectomy (PHx), split-liver transplantation, viral hepatitis, alcoholic hepatitis, and drug-induced liver injury all can induce acute liver injury[1,2]. This susceptibility is particularly pronounced in marginal donor organs characterized by aging, steatosis, or prolonged cold ischemia time. Clinically, R0 resection remains the most effective strategy for treating benign liver tumors and select malignant hepatic lesions. However, insufficient residual liver function following massive PHx often progresses to small-for-size syndrome (SFSS) and post-hepatectomy liver failure (PHLF). The pathological mechanisms underlying "insufficient regeneration" versus "irreversible damage" differ significantly: the former typically manifests as arrested cell cycle initiation or sluggish kinetics-specifically, the inability of hepatocytes to sufficiently regenerate and restore or maintain a critical functional liver mass[3,4]; conversely, the latter is often accompanied by severe programmed cell death, leading to a continuous and precipitous decline in functional hepatocytes within the remnant liver, ultimately resulting in hepatic failure. Although substantial research has accumulated on strategies to promote liver regeneration, their translational outcomes have fallen short of expectations. This suggests that reliance on pro-regenerative approaches alone may be insufficient to overcome the bottleneck of acute liver injury induced by major PHx[5]. Accordingly, research focus has shifted toward "injury-reducing" strategies that identify and intercept the primary drivers of severe acute liver injury. Synergistically integrating these approaches aims to enhance remnant liver viability and ultimately reduce clinical mortality.

Crucially, PHx is not merely a localized surgical event but a trigger for profound systemic metabolic reprogramming. Immediate post-operative demand for energy and membrane components initiates rapid adipose tissue mobilization, flooding the remnant liver with free fatty acids. This results in Transient Regeneration-Associated Steatosis (TRAS)[6,7], a phenomenon traditionally viewed as a vital, temporary energy reservoir fueling the high metabolic costs of hepatocyte proliferation. However, when this lipid influx exceeds the liver's processing capacity or persists abnormally, it may transition from a physiological fuel source to a pathological driver of injury[8,9]. Pyroptosis is a form of pro-inflammatory programmed cell death mediated by the Gasdermin protein family[10,11], which has emerged as a key executioner in this transition. Upon stimulation, NOD-like receptor protein 3 (NLRP3) recruits apoptosis-associated speck-like protein containing a CARD (ASC) to assemble the inflammasome, mediating Caspase-1 activation and the subsequent release of IL-1β[12,13]. Previous reports have demonstrated that inhibiting NLRP3 reduces hepatocyte pyroptosis in acetaminophen (APAP)-induced liver injury models[14]. Furthermore, NLRP3 knockout or pharmacological blockade has been shown to significantly promote liver recovery following PHx[15]. Endoplasmic reticulum stress (ERS), acting as a central hub of cellular stress injury, plays a pivotal role in triggering pyroptosis[16]. The sudden surge in lipid metabolic load during TRAS, compounded by severe ischemia-reperfusion injury[17], and continuous hypoxic hemodynamic shear stress serve as potent disruptors of endoplasmic reticulum (ER) homeostasis[18,19]. Consequently, sustained and intense ERS may transition the liver

from a regenerative state into one of irreversible injury

Glycerophospholipid metabolism serves as the foundation for maintaining ER membrane structural homeostasis. When the proportions of key components such as PC or phosphatidylethanolamine (PE) become dysregulated, ER membrane fluidity is altered[20], directly activating stress sensors like PERK and IRE1α to induce ERS[21]. While the role of PC following PHx is relatively well-defined[22], the drivers of these glycerophospholipid metabolic alterations, their underlying molecular mechanisms, and the specific impact of glycerophospholipid metabolites on injury in the remnant liver require further investigation.

Multi-omics integration offers a novel dimension for dissecting the metabolic remodeling of complex diseases[23]. Joint analysis of transcriptomics, metabolomics, and lipidomics data suggests that bile acid metabolism mediated by FXR (Nuclear Receptor Subfamily 1 Group H Member 4, NR1H4) plays a critical role in post-hepatectomy injury. FXR exerts significant regulatory control over glycerophospholipid metabolism, and while its agonists demonstrate protective effects in liver diseases, they are primarily utilized for primary biliary cholangitis (PBC). Expanding their application requires a deeper understanding of the molecular mechanisms governing their function.

By combining multi-omics data with a machine learning model optimized through 15 algorithms and 207 parameters, we identified death receptor 5 (DR5, also known as TNFRSF10B, TRAIL-R2, or CD262) as a key feature gene regulating glycerophospholipid metabolism after partial hepatectomy. DR5 is a transmembrane

receptor; crucially, its activation can occur intracellularly, independent of its extracellular ligands or TNF-related apoptosis-inducing ligands (TRAIL)[24]. Activation of DR5 regulates downstream effectors-such as FADD, caspase-8, Bid, and caspase-3-playing a vital role in cell injury signal transduction. While DR5 has frequently been targeted in therapies for solid tumors [25,26](including melanoma, breast, lung, and colon cancers). However, studies focused on benign liver disease models are notably scarce[27], particularly regarding hepatocyte injury in the remnant liver after massive hepatectomy, remain unexplored. We observed that significant upregulation of DR5 in the remnant liver hinders the nuclear translocation of FXR, thereby impeding the transcription of Chpt1-a key enzyme in glycerophospholipid metabolism. This results in a PC imbalance, exacerbating ERS and ultimately leading to hepatocyte pyroptosis. Interfering with DR5 expression, activating FXR, and providing supplemental PC all can effectively attenuate pyroptosis, thereby ameliorating acute liver injury following 70% PHx.

In summary, this study utilizes a massive hepatectomy animal model combined with multi-omics analysis and machine learning algorithms to screen for core genes regulating glycerophospholipid metabolism. We investigate how these genes exacerbate ERS and induce hepatocyte pyroptosis by interfering with glycerophospholipid synthesis. This research not only aims to elucidate the molecular mechanisms of irreversible damage after PHx from the perspective of metabolic remodeling but also provides potential therapeutic targets, identified via multi-omics screening, for clinical interventions against unpredictable SFSS or PHLF.

Results

Severe pyroptosis accompanied by profound lipid metabolism dysregulation in the acute injury phase following 70% PHx.

To investigate the injury dynamics of the remnant liver tissue following PHx, we retrospectively collected data from 371 cases, including anatomical left hemihepatectomy (resection volume 30%-40%, n=174), anatomical right hemihepatectomy (resection volume 50%-60%, n=145), and ALPPS (resection volume 60%-70%, n=52). We systematically analyzed postoperative liver enzyme changes after these resection volumes (Figure 1A, Supplementary Figure 1A). The results showed that Alanine Aminotransferase (ALT) levels peaked within 48-72 hours (postoperative day 3, D3) following left hemihepatectomy, right hemihepatectomy, and ALPPS Step-1, indicating an acute injury phase within the first three days. Notably, although the future liver remnant (FLR) regenerates sufficiently after ALPPS Step-1, ALT levels also remained elevated within the first 3 days following Step-2. Other critical indicators of liver function, activated partial thromboplastin time (APTT), albumin (ALB), and total bilirubin (TB), showed significant alterations during this period (Supplementary Figure 1B), confirming an acute injury phase. The probability of developing SFSS or PHLF increased with larger resection volumes (Supplementary Figure 1C). If the histopathological features and molecular pathological alterations during acute liver injury can be elucidated, and the key molecules and pathways critically influencing this injury identified, then targeted interventions could be applied to alleviate damage to the remnant liver following PHx,

thereby substantially reducing the incidence of unpredictable death.

Subsequently, we established 30%, 50% and 70% PHx models in C57BL/6 mice (Figure 1B, Supplementary Figure 1D). Histopathological and serum liver function analyses revealed that the 30% PHx group exhibited minimal injury and minor enzyme fluctuations. The 50% PHx group showed significantly increased injury areas and functional impairment within 3 days compared to the 30% PHx group. The 70% PHx group demonstrated the most severe injury and functional impairment, which progressively worsened over the first 3 days, indicating an acute injury phase. We hypothesized that the progressive exacerbation of remnant liver injury is likely dominated by a specific form of cell death. Therefore, analysis of transcriptomic data across 21 cell death modes revealed that pyroptosis-related genes (PRGs) were among the most significantly upregulated DEGs (Figure 1C, Supplementary Figure 1E). Subsequent GSVA scoring based on these PRGs further confirmed that pyroptosis activity was markedly elevated following 70% PHx at the acute injury phase, reaching its peak at D3 compared to the control and earlier postoperative time points (D1, D2; Figure 1C). Western Blot (WB) analysis confirmed significant upregulation of pyroptosis-associated proteins at the acute injury phase (Figure 1D, Supplementary Figure 1F). ELISA results confirmed that IL-1β and IL-18 were significantly upregulated at the acute phase (Figure 1E). Scanning Electron Microscopy (SEM) revealed extensive membrane pore formation on hepatocytes in the remnant liver at D3, Transmission Electron Microscopy (TEM) indicated severe disruption of mitochondrial and endoplasmic reticulum (ER) structures compared to controls: both

organelles exhibited marked swelling and membrane rupture (Figure 1F). Specifically, D3 samples showed severe destruction of mitochondrial structures and ER disintegration.

To amplify this process, we established a 90% PHx model in C57BL/6 mice. Single-cell RNA sequencing (scRNA-seq) at the D3 revealed that, compared with 70% PHx, hepatocyte injury was substantially increased in the remnant liver after 90% PHx, with prominent upregulation of PRGs in hepatocytes. Consistently, the GSVA pyroptosis score in hepatocytes was markedly elevated relative to that in the 70% PHx group (Supplementary Figure 1G). These findings suggest that excessive activation of pyroptosis likely drives more severe liver injury. Prompted by the observation of pronounced vacuolization in H&E staining sections and increased lipid droplets under TEM, we performed Oil Red O staining, which confirmed a significant accumulation of intrahepatic lipids following 70% PHx (Figure 1G). Furthermore, RNA-seq analysis of the 70% PHx model revealed that significantly upregulated PRGs were also involved in regulating lipid metabolism pathways (Figure 1H). Consistent findings were observed among the upregulated PRGs in hepatocytes identified by scRNA-seq in the 90% PHx compared to the 70% PHx (Supplementary Figure 1H-J). These results strongly suggest that severe pyroptosis occurs, accompanied by significant dysregulation of lipid metabolism in the acute injury phase following 70% PHx.

Disruptions in lipid metabolism may contribute to the induction of pyroptosis.

As the body's primary metabolic organ, the liver plays a pivotal role in

maintaining systemic homeostasis, and its dysfunction can exert profound and far-reaching effects on whole-body physiological stability. Therefore, we further explored the acute-phase pathophysiological alterations and identify potential triggers of pyroptosis. The expression of lipid import genes (*Cd36, Fabp2*) and lipid droplet formation genes (*Plin2*) significantly increased, while lipid synthesis genes (*Acaca, Fasn, Scd1*) significantly decreased. Conversely, genes related to lipid consumption (*Cpt1-α, Acadm, Acads, Crat, Hadhb*) were elevated (Figure 2A, Supplementary Figure 2A-G). Integrating our experimental findings with prior literature, energy requirements are primarily fulfilled through β-oxidation of imported lipids, without a corresponding increase in de novo lipid synthesis following 70% PHx. This imbalance leads to substantial lipid accumulation in remnant hepatocytes, and such dysregulation of lipid metabolism is highly likely to underlie the observed injury. LC-MS quantitative lipidomics at various time points showed a significant elevation in free fatty acids (FFAs) within 3 days post-PHx, with Palmitic Acid (PA) occupying the largest proportion (Figure 2B-C). To simulate these conditions in vitro, THLE-2 hepatocytes were cultured with increasing concentrations of PA. Higher PA concentrations significantly inhibited cell proliferation (Supplementary Figure 2H-J) and induced progressive pyroptosis (Figure 2D, Supplementary Figure 2K). Considering the ischemia-reperfusion injury and continuous hypoxic portal flow from the gut during PHx, we added hypoxia treatment to the 0.25mmol/L PA condition to better mimic the hepatic microenvironment. Light microscopy revealed exacerbated cell injury in the Hypoxia+PA group (Figure 2E), and CCK-8 assays showed

significantly reduced viability (Figure 2F). WB results confirmed more severe pyroptosis in the Hypoxia+PA group (Figure 2G, Supplementary Figure 2L). To validate whether lipid burden causes pyroptosis, we treated 70% PHx models with WY-14643 (to reduce intracellular FFAs) and Etomoxir (ETO, to inhibit β-oxidation and increase intracellular FFAs) (Figure 2H). Remarkably, WY-14643 treatment significantly reduced the injury area and improved liver function, whereas ETO treatment significantly increased the injury area (Figure 2I-J) and worsened liver function (Figure 2K, Supplementary Figure 2M). Consistent with their mechanisms, WY-14643 significantly lowered intrahepatic FFAs levels, while ETO elevated them (Figure 2L). WB analysis showed that WY-14643 downregulated, while ETO upregulated, pyroptosis-related proteins (Figure 2M, Supplementary Figure 2N). Furthermore, WY-14643 effectively improved survival in a 90% PHx model (Figure 2N), while ETO significantly reduced survival in the 70% PHx model (Figure 2O).These findings suggest that lipid metabolism disorder is a likely cause of pyroptosis post-hepatectomy.

PC supplementation effectively mitigates ERS, thereby reducing hepatocyte pyroptosis following 70% PHx.

To pinpoint the specific lipid types affecting pyroptosis, we analyzed lipidomics data. Of 1474 detected lipids, 733 showed significant daily changes within the first 3 days post-70% PHx, with glycerolipids emerging as particularly prominent (Supplementary Figure 3A). Pseudotime analysis revealed three subclasses (Figure

3A): Subclass 1 was dominated by rising PE (Supplementary Figure 3B); Subclass 2 showed similar PC and PE changes (Supplementary Figure 3C); Subclass 3 showed the most significant downregulation of PC, correlating closely with glycerophospholipid metabolism (Figure 3B-C). As a key component of cellular membranes, PC deficiency likely compromises membrane fluidity and stability, triggering ERS and cellular injury. In vitro supplementation with exogenous PC effectively protected cells against hypoxia and lipid accumulation-induced injury, reduced oxidative lipids, increased viability (Figure 3D-E), alleviated ERS (Figure 3F-G), and consequently reduced pyroptosis (Figure 3H, Supplementary Figure 3D). Consistent with these in vitro findings, in vivo PC supplementation ameliorated functional deterioration in the remnant liver after 70% PHx (Figure 3I–J, Supplementary Figure 3E). SEM revealed reduced membrane pore formation, while TEM demonstrated mitigated mitochondrial swelling with preserved membrane and cristae architecture; ER dilation was markedly relieved, yielding clearer overall ultrastructure compared to controls (Figure 3K). H&E staining showed a significant decrease in the proportion of injured tissue and reduced intracellular oxidative lipids following PC supplementation (Figure 3L–M). qRT-PCR and WB further confirmed that PC supplementation alleviated ER stress and consequently diminished pyroptosis (Figure 3O–P, Supplementary Figure 3F). Collectively, PC depletion exerts a profound influence on pyroptosis, and its supplementation effectively mitigates ER stress, thereby reducing hepatocyte pyroptosis after PHx.

DR5 is a key gene driving pyroptosis after 70% PHx.

To identify the key gene driving pyroptosis and providing a therapeutic target, we analyzed transcriptomic data, identifing 3375 DEGs (2226 upregulated, 1149 downregulated) in the first 3 days (Figure 4A). Weighted Gene Co-expression Network Analysis (WGCNA) grouped all genes into 18 modules, which were merged into 6 distinct modules based on similarity (Figure 4B). The Brown and Green modules showed high Pearson correlation coefficients (>0.7) with PHx, suggesting their importance (Figure 4C). Using single-cell data from a public database (CNP0002310)[28], we identified DEGs in hepatocytes across time points (Figure 4D) and intersected them with transcriptomic DEGs and PRGs, yielding 26 candidate genes (Figure 4E). Machine learning algorithms were employed to determine the most critical gene (Supplementary Figure 4A-B). The top 10 genes by importance were *Lcn2, Dnmt1, DR5, Ccnd1, Anxa2, Pkm, Prim1, Tubb6, Btg3, and Flot1* (Figure 4F, Supplementary Figure 4). Death Receptor 5 (DR5) consistently ranked high across multiple models, highlighting its potential causal link to liver injury. A similar approach identified 20 lipid metabolism-related genes (Supplementary Figure 5A), where DR5 also ranked highly (Supplementary Figure 5B-D). Validation via qRT-PCR and WB showed elevated DR5 expression in both animal and cell models (Figure 4G-H, Supplementary Figure 5E). Knockdown of DR5 in THLE-2 cells significantly reduced pyroptosis-related protein expression (Figure 4I, Supplementary Figure 5F). In human ALPPS samples, DR5 expression was significantly higher in liver tissue from the second stage surgery compared to the first (Figure 4J-M).

Retrospective analysis revealed that patients with high DR5 expression had significantly elevated ALT and AST levels following Step 2 (Figure 4N, Supplementary Figure 5G), and DR5 expression positively correlated with serum ALT and AST on postoperative day 1 (POD1) (Figure 4O, Supplementary Figure 5H).

DR5 promotes pyroptosis by impeding nuclear translocation of FXR.

To elucidate the molecular mechanism by which DR5 drives pyroptosis, we performed proteomics profiling of the remnant liver at multiple time points post-PHx. A total of 6579 proteins were detected, of which 2875 exhibited significant daily fluctuations within the first 3 days (Figure 5A). Functions were enriched in lipid transport and metabolism, predominantly localizing to the cytoplasm (Supplementary Figure 6A). Pseudotime analysis identified 6 Subclasses (Figure 5B). Subclass 3, which mirrored the PC trend, was closely related to lipid metabolism (Figure 5C) and cytoplasmic localization (Figure 5D). Notably, CHPT1 (Choline Phosphotransferase 1), a key enzyme for PC synthesis, belonged to Subclass 3 (Figure 5E). WB confirmed sustained downregulation of CHPT1 post-PHx (Figure 5F, Supplementary Figure 6D). CO-IP assays indicated no direct interaction between DR5 and CHPT1 (Figure 5G). Multi-omics integration (Metabolomics+Proteomics+Transcriptomics) pointed towards primary bile acid synthesis as a central functional node (Figure 5H, Supplementary Figure 6E-F). This suggested FXR (a regulator of bile acid synthesis) as a potential link. Nuclear-cytoplasmic fractionation assays revealed that as cytoplasmic DR5 levels rose, nuclear FXR significantly decreased (Figure 5I,

Supplementary Figure 6G). Immunofluorescence (IF) confirmed that increased DR5 expression in cell models correlated with reduced nuclear FXR (Figure 5J, Supplementary Figure 6H). Conversely, DR5 knockdown (DR5-KD) restored FXR nuclear translocation (Figure 5K, Supplementary Figure 6I). Functionally, both DR5-KD and the FXR agonist GW4064 effectively reduced pyroptosis in THLE-2 cells, with synergistic effects when combined (Figure 5L, Supplementary Figure 6J). DR5 overexpression (DR5-OE) increased pyroptosis, which was mitigated by GW4064 (Figure 5M, Supplementary Figure 6K). The FXR antagonist Z-GS exacerbated pyroptosis, an effect attenuated by DR5-KD but aggravated by DR5-OE (Figure 5N, Supplementary Figure 6L). These findings confirm that DR5 promotes pyroptosis by hindering FXR nuclear translocation.

The DR5-FXR-CHPT1 axis regulates pyroptosis after 70% PHx.

We next investigated how FXR regulates *Chpt1*. In cell models, DR5-KD or GW4064 treatment significantly increased CHPT1 protein levels (Figure 6A, Supplementary Figure 7A). Conversely, DR5-OE downregulated CHPT1, an effect rescued by GW4064 (Figure 6B, Supplementary Figure 7B). The FXR antagonist Z-GS potentiated the DR5-OE inducing downregulation of CHPT1 (Figure 6C, Supplementary Figure 7C), confirming that DR5 regulates CHPT1 via FXR activity. FXR is a transcription factor, JASPAR analysis visualized its preferred DNA binding motif (Figure 6D). Integration of GTRD, TCGA, GTEx, and ChIP-Atlas databases indicated *Chpt1* is a target of FXR (Figure 6E). We identified a clear FXR binding

peak in the *Chpt1* promoter region enriched with the H3K27Ac enhancer mark. ChIP-qPCR confirmed that GW4064 treatment significantly upregulated *Chpt1* transcription, verifying direct positive regulation (Figure 6F). Analysis of GTEx, TCGA, and CCLE databases showed a significant positive correlation between FXR (NR1H4) and CHPT1 expression in normal tissues (Figure 6G, Supplementary Figure 7D-E). In human ALPPS samples, SFSS patients exhibited significantly upregulated DR5 and reduced FXR/CHPT1 colocalization and expression compared to those with smooth recovery (Figure 6H).To validate the axis in vivo, we utilized an AAV-DR5 knockdown vector with verified liver targeting in the 70% PHx model (Figure 6I, Supplementary Figure 7F-G). Treatment with AAV-DR5 or GW4064 significantly decreased ALT and AST levels (Figure 6J, Supplementary Figure 7H) and reduced liver injury (Figure 6K-L). However, FXR inhibition with Z-GS exacerbated injury and nullified the protective effects of AAV-DR5 and GW4064. SEM and TEM showed that Z-GS treatment induced severe membrane pore formation, sinusoidal congestion, and mitochondrial swelling, whereas AAV-DR5 or GW4064 maintained organelle integrity. Western blots showed that Z-GS downregulated CHPT1 and upregulated pyroptosis markers, while AAV-DR5 or GW4064 upregulated CHPT1 and suppressed pyroptosis (Figure 6M). In summary, activating FXR increases the transcription of CHPT1, thereby enhancing PC generation, balancing ERS, and inhibiting hepatocyte pyroptosis (Figure 7). The DR5-FXR-CHPT1 axis is a potent hepatoprotective pathway regulating injury after 70% PHx.

Discussion

In this study, we employed a large-volume PHx animal models combined with multi-omics analysis and machine learning to elucidate the potential causes and molecular mechanisms underlying the unpredictable and severe injury (PHLF and SFSS) following liver resection. We revealed that pyroptosis driven by endoplasmic reticulum stress (ERS) is a critical factor leading to functional decompensation of the remnant liver. Crucially, we identified and validated a novel metabolic-inflammatory regulatory axis driven by DR5: the aberrant upregulation of DR5 induced by massive PHx impedes FXR nuclear translocation and inhibits CHPT1 transcription. This disrupts glycerophospholipid metabolic homeostasis and compromises ER membrane stability, thereby exacerbating ERS and progressing to lethal hepatocyte pyroptosis. These findings have prompted us to expand the intervention strategy for postoperative PHLF and SFSS from purely "promoting regeneration" to "reducing injury," further breaking the bottleneck in treating acute liver injury induced by large-volume hepatectomy.

PHx triggers systemic metabolic changes, particularly adipose tissue mobilization[29,30]. While transient regeneration-associated steatosis (TRAS) is recognized as an energy source for regeneration[7,31]. Our lipidomics data further reveal a persistent and substantial lipid burden in the liver during the first three days following 70% PHx. This burden is exacerbated by perioperative pathophysiological changes associated with liver resection, including ischemia-reperfusion injury, whereby the remnant liver must rapidly assume full functional load; elevated portal

venous pressure[32]; dysregulated blood flow redistribution in the remnant liver[33], leading to increased perfusion with hypoxic blood, and potential effective circulating volume insufficiency due to reduced hepatic vascular bed[17,34]. These factors collectively predispose the remnant liver to irreversible injury. When we reduced this lipid burden using WY-14643, remnant liver injury was mitigated, and survival in 90% PHx models improved. Conversely, exacerbating the lipid burden with ETO worsened injury and survival. Sustained excessive lipid input brings a massive lipid burden that first triggers ERS by reducing ER membrane fluidity, disrupting calcium homeostasis, and inducing oxidative damage, which directly interferes with protein folding. When the stressed ER attempts to restore balance, it often paradoxically activates lipid synthesis transcription factors, leading to further intracellular lipid accumulation[20]. This pathological feedback loop of "lipotoxicity-induced stress, and stress-exacerbated accumulation" likely culminates in severe damage to remnant hepatocytes[35].

We found that pyroptosis is the primary type of cell death leading to severe remnant hepatocyte injury. This form of programmed cell death, mediated by caspase-1 and accompanied by the release of IL-1β and IL-18, triggers a robust inflammatory response. While its participation in tissue injury during liver ischemia-reperfusion and steatosis has been confirmed[36,37], its role in hepatocyte injury induced by lipid metabolism imbalance after massive PHx remains unclear, particularly its association with glycerophospholipid metabolic disorders. Glycerophospholipids are not only major components of cell and organelle

membranes but are also linked to neuroinflammatory levels[38]; maintaining glycerophospholipid metabolic homeostasis in the brain is key to inhibiting neuroinflammation and delaying cognitive decline. Upregulated PC levels help improve lipid deposition in non-alcoholic fatty liver disease (NAFLD) and reduce hepatic steatosis, indicating that the stability of glycerophospholipid metabolism is an important pathway for maintaining metabolic homeostasis[39]. Our lipidomics data show that glycerophospholipid metabolism is extremely important in 70% PHx. Notably, exogenous PC supplementation in the 70% PHx markedly attenuated remnant hepatocyte pyroptosis. Severe ERS triggered by glycerophospholipid dysregulation likely promotes NLRP3 inflammasome assembly and Caspase-1 activation. This mechanism not only explains the frequent association of SFSS with severe systemic inflammatory response syndrome in clinical practice but also accounts for the limited efficacy of anti-inflammatory therapies alone-persistent inflammation arises from uncorrected upstream defects in membrane lipid metabolism. Our findings align with previous reports that NLRP3 knockout enhances liver regeneration while providing the missing upstream metabolic trigger.

Through the integration of multi-omics data and machine learning, we precisely identified DR5 as a core gene regulating glycerophospholipid metabolism, filtering out noise inherent in traditional screening. This data-driven approach allowed us to redefine the role of DR5 in non-neoplastic liver injury. Unlike its classical role as a receptor for TRAIL in inducing tumor apoptosis[25,40], we demonstrate that in the context of post-hepatectomy pathology, DR5 acts as a key upstream "molecular

switch" for metabolic reprogramming. Crucially, we found that DR5 activation after PHx occurs intracellularly, independent of extracellular ligands. This non-canonical function expands the biological understanding of the death receptor family and explains why DR5 exerts significant pathological control even in sterile surgical injury lacking exogenous immune attack.

At the mechanistic level, we established a causal link between signal transduction and organellar membrane homeostasis via the “DR5–FXR–CHPT1” axis. Dynamic balance between PC and PE ratios is essential for membrane fluidity and ER function. Our data show that DR5-mediated impairment of FXR nuclear translocation directly suppresses transcription of CHPT1, the rate-limiting enzyme in PC synthesis. Intriguingly, the FXR agonist GW4064 markedly upregulated both CHPT1 transcription and protein expression. Comprehensive validation using DR5 knockdown or overexpression combined with FXR agonists and inhibitors confirmed the functional integrity of the “DR5–FXR–CHPT1” axis. Injury arising from metabolic substrate deficiency is more refractory to reversal than conventional protein folding overload, leading to sustained hyperactivation of stress sensors and conversion of the normally adaptive unfolded protein response (UPR) into toxic pro-death signaling[41].

From a translational perspective, this study offers novel metabolism-targeted strategies for preventing and treating PHLF and SFSS, conditions currently lacking specific therapeutic targets. Our findings suggest that targeting the DR5–FXR axis or directly modulating glycerophospholipid metabolism holds therapeutic promise.

Exogenous PC supplementation or pharmacological FXR activation to restore CHPT1 expression could stabilize ER membrane architecture in the remnant liver, thereby interrupting the vicious “ERS–pyroptosis” cycle. We validated this pathway in animal models and human ALPPS specimens. However, SFSS involves more complex portal hemodynamics and inter-individual metabolic variability[42]; thus, the clinical relevance of the DR5–FXR axis requires further validation in larger cohorts. Additionally, whether glycerophospholipid regulation of pyroptosis is hepatocyte-specific and involves interactions with the hepatic immune microenvironment remains to be clarified[43]. The optimal therapeutic window for intervening in this pathway also warrants future investigation.

In summary, this study uncovers a novel mechanism whereby DR5 disrupts ER membrane homeostasis and induces hepatocyte pyroptosis by suppressing the key glycerophospholipid synthetic enzyme CHPT1. The identification of the DR5–metabolism–pyroptosis axis provides a new theoretical framework for understanding impaired injury recovery after massive PHx, nominates potential molecular targets for preventing and treating lethal PHLF, and lays a foundational basis for developing novel metabolism-targeted hepatoprotective therapeutics.

References

1 Forbes, S. J. & Newsome, P. N. Liver regeneration - mechanisms and models to clinical application. *Nat Rev Gastroenterol Hepatol* **13**, 473-485, doi:10.1038/nrgastro.2016.97 (2016).

2 Campana, L., Esser, H., Huch, M. & Forbes, S. Liver regeneration and inflammation: from fundamental science to clinical applications. *Nat Rev Mol Cell Biol* **22**, 608-624, doi:10.1038/s41580-021-00373-7 (2021).

3 Lehmann, K. *et al.* Liver failure after extended hepatectomy in mice is mediated by a p21-dependent barrier to liver regeneration. *Gastroenterology* **143**, 1609-1619 e1604, doi:10.1053/j.gastro.2012.08.043 (2012).

4 Sun, S. *et al.* Advanced oxidation protein products induce S-phase arrest of hepatocytes via the ROS-dependent, beta-catenin-CDK2-mediated pathway. *Redox Biol* **14**, 338-353, doi:10.1016/j.redox.2017.09.011 (2018).

5 Zwirner, S. *et al.* First-in-class MKK4 inhibitors enhance liver regeneration and prevent liver failure. *Cell* **187**, 1666-1684 e1626, doi:10.1016/j.cell.2024.02.023 (2024).

6 Dong, Q. *et al.* Adipose tissue deficiency impairs transient lipid accumulation and delays liver regeneration following partial hepatectomy in male Seipin knockout mice. *Clin Transl Med* **15**, e70238, doi:10.1002/ctm2.70238 (2025).

7 Kachaylo, E. *et al.* PTEN Down-Regulation Promotes beta-Oxidation to Fuel Hypertrophic Liver Growth After Hepatectomy in Mice. *Hepatology* **66**, 908-921, doi:10.1002/hep.29226 (2017).

8 Lee, E., Korf, H. & Vidal-Puig, A. An adipocentric perspective on the development and progression of non-alcoholic fatty liver disease. *J Hepatol* **78**, 1048-1062, doi:10.1016/j.jhep.2023.01.024 (2023).

9 Azzu, V., Vacca, M., Virtue, S., Allison, M. & Vidal-Puig, A. Adipose Tissue-Liver Cross Talk in the Control of Whole-Body Metabolism: Implications in Nonalcoholic Fatty Liver Disease. *Gastroenterology* **158**, 1899-1912, doi:10.1053/j.gastro.2019.12.054 (2020).

10 Broz, P., Pelegrin, P. & Shao, F. The gasdermins, a protein family executing cell death and inflammation. *Nat Rev Immunol* **20**, 143-157, doi:10.1038/s41577-019-0228-2 (2020).

11 Shi, J., Gao, W. & Shao, F. Pyroptosis: Gasdermin-Mediated Programmed Necrotic Cell Death. *Trends Biochem Sci* **42**, 245-254, doi:10.1016/j.tibs.2016.10.004 (2017).

12 C. Yu, P. C., L. Miao, G. Di. the role of the NLRP3 inflammasome and programmed cell death in acute liver injury. *Int. J. Mol. Sci*, doi:10.3390/ijms24043067 (2023).

13 T. Ye, W. Y. T., X. Y. Chen, C. Jiang, B. Di, L. L. Xu. Mechanisms of NLRP3 inflammasomeactivation and the development of peptide inhibitors. *Cytokine Growth Factor Rev*, doi:10.1016/j.cytogfr.2023.09.007 (2023).

14 Yuan, X. *et al.* NLRP3 deficiency protects against acetaminophen-induced liver injury by inhibiting hepatocyte pyroptosis. *Mol Med Rep* **29**, doi:10.3892/mmr.2024.13185 (2024).

15 Wei, S. *et al.* NLRP3 inflammasome constrains liver regeneration through impairing MerTK-mediated macrophage efferocytosis. *Sci Adv* **11**, eadq5786, doi:10.1126/sciadv.adq5786 (2025).

16 Ong, G. *et al.* IRE1 signaling increases PERK expression during chronic ER stress. *Cell Death Dis* **15**, 276, doi:10.1038/s41419-024-06663-0 (2024).

17 Tang, Y. *et al.* RAMP1 Protects Hepatocytes against Ischemia-reperfusion Injury by Inhibiting

the ERK/YAP Pathway. *J Clin Transl Hepatol* **12**, 357-370, doi:10.14218/JCTH.2023.00339 (2024).

18 Lebeaupin, C. *et al.* ER stress induces NLRP3 inflammasome activation and hepatocyte death. *Cell Death Dis* **6**, e1879, doi:10.1038/cddis.2015.248 (2015).

19 Ajoolabady, A. *et al.* Endoplasmic reticulum stress in liver diseases. *Hepatology* **77**, 619-639, doi:10.1002/hep.32562 (2023).

20 Fu, S. *et al.* Aberrant lipid metabolism disrupts calcium homeostasis causing liver endoplasmic reticulum stress in obesity. *Nature* **473**, 528-531, doi:10.1038/nature09968 (2011).

21 Qiu, Y. *et al.* A Lipid Perspective on Regulated Pyroptosis. *Int J Biol Sci* **19**, 2333-2348, doi:10.7150/ijbs.81017 (2023).

22 Ling, J., Chaba, T., Zhu, L. F., Jacobs, R. L. & Vance, D. E. Hepatic ratio of phosphatidylcholine to phosphatidylethanolamine predicts survival after partial hepatectomy in mice. *Hepatology* **55**, 1094-1102, doi:10.1002/hep.24782 (2012).

23 Liu, Z. *et al.* Machine learning-enhanced discovery of a basement membrane-related gene signature in glioblastoma via single-cell and Spatial transcriptomics. *J Transl Med* **23**, 1325, doi:10.1186/s12967-025-06918-0 (2025).

24 Lu, M. *et al.* Opposing unfolded-protein-response signals converge on death receptor 5 to control apoptosis. *Science* **345**, 98-101, doi:10.1126/science.1254312 (2014).

25 Guo, Y. *et al.* Engineered extracellular vesicles with DR5 agonistic scFvs simultaneously target tumor and immunosuppressive stromal cells. *Sci Adv* **11**, eadp9009, doi:10.1126/sciadv.adp9009 (2025).

26 Li, J. *et al.* Combination of multivalent DR5 receptor clustering agonists and histone deacetylase inhibitors for treatment of colon cancer. *J Control Release* **376**, 1014-1024, doi:10.1016/j.jconrel.2024.10.062 (2024).

27 Wang, Y. *et al.* DR5 Governs Compound Exocytosis in Colonic Goblet Cells via TATA-Box Binding Protein-Dependent Bestrophin-2 Transcriptional Regulation. *Adv Sci (Weinh)* **13**, e16789, doi:10.1002/advs.202516789 (2026).

28 Xu, J. *et al.* A spatiotemporal atlas of mouse liver homeostasis and regeneration. *Nat Genet* **56**, 953-969, doi:10.1038/s41588-024-01709-7 (2024).

29 Lund, A. *et al.* Role of Steatosis in Preventing Post-hepatectomy Liver Failure After Major Resection: Findings From an Animal Study. *J Clin Exp Hepatol* **15**, 102453, doi:10.1016/j.jceh.2024.102453 (2025).

30 Chen, Y. *et al.* Acute liver steatosis translationally controls the epigenetic regulator MIER1 to promote liver regeneration in a study with male mice. *Nat Commun* **14**, 1521, doi:10.1038/s41467-023-37247-9 (2023).

31 Zhang, L. *et al.* mTORC2 Facilitates Liver Regeneration Through Sphingolipid-Induced PPAR-alpha-Fatty Acid Oxidation. *Cell Mol Gastroenterol Hepatol* **14**, 1311-1331, doi:10.1016/j.jcmgh.2022.07.011 (2022).

32 Bogner, A. *et al.* Intraoperative Increase of Portal Venous Pressure is an Immediate Predictor of Posthepatectomy Liver Failure After Major Hepatectomy: A Prospective Study. *Ann Surg* **274**, e10-e17, doi:10.1097/SLA.0000000000003496 (2021).

33 Cho, J. Y. *et al.* Association of Remnant Liver Ischemia With Early Recurrence and Poor Survival After Liver Resection in Patients With Hepatocellular Carcinoma. *JAMA Surg* **152**,

386-392, doi:10.1001/jamasurg.2016.5040 (2017).

34 Dili, A., Bertrand, C., Lebrun, V., Pirlot, B. & Leclercq, I. A. Hypoxia protects the liver from Small For Size Syndrome: A lesson learned from the associated liver partition and portal vein ligation for staged hepatectomy (ALPPS) procedure in rats. *Am J Transplant* **19**, 2979-2990, doi:10.1111/ajt.15420 (2019).

35 Celik, C., Lee, S. Y. T., Yap, W. S. & Thibault, G. Endoplasmic reticulum stress and lipids in health and diseases. *Prog Lipid Res* **89**, 101198, doi:10.1016/j.plipres.2022.101198 (2023).

36 Kolachala, V. L., Lopez, C., Shen, M., Shayakhmetov, D. & Gupta, N. A. Ischemia reperfusion injury induces pyroptosis and mediates injury in steatotic liver thorough Caspase 1 activation. *Apoptosis* **26**, 361-370, doi:10.1007/s10495-021-01673-1 (2021).

37 Liu, Y., Li, S., Zhang, G. & Cai, J. NOD1 induces pyroptotic cell death to aggravate liver ischemia-reperfusion injury in mice. *MedComm (2020)* **3**, e170, doi:10.1002/mco2.170 (2022).

38 Qian, X. *et al.* Multi-omics data reveals aberrant gut microbiota-host glycerophospholipid metabolism in association with neuroinflammation in APP/PS1 mice. *Gut Microbes* **15**, 2282790, doi:10.1080/19490976.2023.2282790 (2023).

39 Bai, Y. *et al.* Lipid Nanoparticle-Mediated Delivery of CRISPR-Cas9 Against Rubicon Ameliorates NAFLD by Modulating CD36 Along with Glycerophospholipid Metabolism. *Adv Sci (Weinh)* **11**, e2400493, doi:10.1002/advs.202400493 (2024).

40 Wang, H. *et al.* DR5 CAR-T cells target melanoma and suppress MDSCs with minimal toxicity. *Mol Ther*, doi:10.1016/j.ymthe.2025.12.025 (2025).

41 Livezey, M., Huang, R., Hergenrother, P. J. & Shapiro, D. J. Strong and sustained activation of the anticipatory unfolded protein response induces necrotic cell death. *Cell Death Differ* **25**, 1796-1807, doi:10.1038/s41418-018-0143-2 (2018).

42 Law, J. H. & Kow, A. W. Prediction and management of small-for-size syndrome in living donor liver transplantation. *Clin Mol Hepatol* **31**, S301-S326, doi:10.3350/cmh.2024.0870 (2025).

43 Liang, D., Minikes, A. M. & Jiang, X. Ferroptosis at the intersection of lipid metabolism and cellular signaling. *Mol Cell* **82**, 2215-2227, doi:10.1016/j.molcel.2022.03.022 (2022).

44 Mitchell, C. & Willenbring, H. A reproducible and well-tolerated method for 2/3 partial hepatectomy in mice. *Nat Protoc* **3**, 1167-1170, doi:10.1038/nprot.2008.80 (2008).

45 Sun, M. *et al.* Phosphatidylcholine Enhances Homeostasis in Peach Seedling Cell Membrane and Increases Its Salt Stress Tolerance by Phosphatidic Acid. *Int J Mol Sci* **23**, doi:10.3390/ijms23052585 (2022).

46 Yang, J. *et al.* Peroxisome proliferator-activated receptor alpha agonist induces mouse hepatomegaly through the spatial hepatocyte enlargement and proliferation. *Acta Pharmacol Sin* **44**, 2037-2047, doi:10.1038/s41401-023-01096-5 (2023).

47 Divakaruni, A. S. *et al.* Etomoxir Inhibits Macrophage Polarization by Disrupting CoA Homeostasis. *Cell Metab* **28**, 490-503 e497, doi:10.1016/j.cmet.2018.06.001 (2018).

48 Zheng, Y. *et al.* Activation of Pancreatic Acinar FXR Protects against Pancreatitis via Osgin1-Mediated Restoration of Efficient Autophagy. *Research (Wash D C)* **2022**, 9784081, doi:10.34133/2022/9784081 (2022).

49 Han, C. Y. *et al.* FXR Inhibits Endoplasmic Reticulum Stress-Induced NLRP3 Inflammasome in Hepatocytes and Ameliorates Liver Injury. *Cell Rep* **24**, 2985-2999, doi:10.1016/j.celrep.2018.07.068 (2018).

50 Huang, P. *et al.* FXR deficiency induced ferroptosis via modulation of the CBP-dependent p53 acetylation to suppress breast cancer growth and metastasis. *Cell Death Dis* **15**, 826, doi:10.1038/s41419-024-07222-3 (2024).

Acknowledgments

The authors would like to acknowledge the technical assistance provided by the staff of the Department of Hepatic Surgery, Liver Transplantation Center, the Third Affiliated Hospital of Sun Yat-sen University, Guangzhou, China.

Author contributions

H.L., C.J., Y.T. and Z.Y. conceived and designed the study. Y.T., X.L. and X.L. performed the experiments. X.L., L.Y. and Q.L. analyzed the data. Y.S., Z.Q., M.K. and Z.R. contributed reagents and material tools. Y.T. and C.J. drafted the manuscript. All of the authors reviewed and edited the manuscript.

Financial support statement

This work was supported by The National Natural Science Foundation of China (No. 82270688 to Hua Li, No. 81402426 to Changchang Jia); The Natural Science Foundation of Guangdong Province (No. 2022A1515012650 to Changchang Jia); The Cultivation Project of National Natural Science Foundation of the Third Affiliated Hospital of Sun Yat-sen University (No. 2020GZRPYMS09 to Changchang Jia); Science and Technology Program of Guangzhou (No. 2023A04J1802 to Zenan Yuan); Key Research and Development Program of Guangzhou Science and Technology Plan

(No. 2024B03J1338 to Hua Li); The “Five-Five” Project of Third Affiliated Hospital of Sun Yat-sen University (No. 2023WW105 to Hua Li).

Conflict of interest

The authors have no conflict of interests related to this publication.

Data sharing statement

The datasets generated during and/or analyzed during the study are available from the corresponding author on reasonable request.

Ethical statement

All animal procedures were approved by the Institutional Animal Care and Use Committee (IACUC), Sun Yat-Sen University (SYSU-IACUC-2025-001978). This study was approved by the Clinical Research Ethics Committee of the Third Affiliated Hospital of Sun Yat-sen University (Ⅱ2025-316-1). All participants were informed about the study and provided written informed consent before inclusion.

Figure legend

Figure 1. Severe pyroptosis accompanied by profound lipid metabolism dysregulation in the acute injury phase following 70% PHx.

A: Serum ALT levels following anatomical left hemihepatectomy, anatomical right hemihepatectomy and ALPPS. B: Representative H&E staining images of liver tissue

from mice with different resection volumes (30%, 50%, and 70%) (Scale bar = 200 μm); Quantification of the percentage of liver injury area in mice with different resection volumes at various postoperative time points; Serum ALT levels in mice with different resection volumes at various postoperative time points. C: Classification of cell death patterns derived from RNA-seq DEGs of liver tissue at D3 following 70% PHx; GSVA scores for DEGs and PRGs in liver tissues from 70% PHx mice. D: Western blot analysis of pyroptosis-related proteins in liver tissue following 70% PHx. E: Serum levels of IL-1β and IL-18 cytokines measured by ELISA following 70% PHx. F: Representative Transmission Electron Microscopy (TEM) and Scanning Electron Microscopy (SEM) images of liver tissue following 70% PHx (Scale bar = 10 μm). G: Representative Oil Red O staining images of liver tissue following 70% PHx (Scale bar = 200 μm). H: Venn diagram identifying the intersection of upregulated PRGs across lipid, glucose, and amino acid metabolic pathways in 70% PHx RNA-seq; KEGG enrichment analysis of upregulated PRGs from 70% PHx RNA-seq. Abbreviations: DEGs, differently expressed genes; PRGs: pyroptosis-related genes; GSVA, gene set variation analysis; SEM, scanning electron microscopy; TEM, transmission electron microscopy; Statistical analysis: All quantitative data are presented as Mean ± SD. Statistical significance was determined by one-way ANOVA. Ns: not significant, $*p < 0.05$, $**p < 0.01$, $***p < 0.001$, and $****p < 0.0001$.

Figure 2. Disordered lipid metabolism triggers pyroptosis following 70% PHx.

A: Expression trends of lipid metabolism-related genes in mouse liver tissue

following 70% PHx. B: Lipidomic profiling of lipid contents in liver tissue at different time points following 70% PHx. C: FFAs and PA contents in lipidomics analysis. D: Western blot analysis of pyroptosis-related proteins in cells treated with different concentrations of PA. E: Representative images of cell morphology and density under combined H+PA treatment (Scale bar = 10 μm). F: Cell viability assessed by CCK-8 assay under different treatment conditions. G: Western blot analysis of pyroptosis-related proteins in the cell model. K:Schematic diagram of the experimental design. H: Schematic diagram of the experimental design. I: Representative H&E images of liver tissue from each groups following 70% PHx. J: Quantification of the percentage of liver injury area in each group following 70% PHx. K: Serum ALT levels in each group following 70% PHx. L: Statistical analysis of FFAs content in liver tissue at D3 post-70% PHx. M: Western blot analysis of pyroptosis-related proteins in liver tissue at D3 post-70% PHx. N: Survival curve of the 90% PHx treated with WY-14643. O: Survival curve of the 70% PHx treated with ETO. Abbreviations: ETO, Etomoxir; Statistical analysis: All quantitative data are presented as Mean ± SD. Statistical significance was determined by one-way ANOVA. Ns: not significant, *$p < 0.05$, **$p < 0.01$, ***$p < 0.001$, and ****$p < 0.0001$.

Figure 3. PC supplementation alleviates ERS and reduces post-70% PHx pyroptosis.

A: Pseudotime analysis of differential lipid components following 70% PHx. B: KEGG pathway enrichment analysis of Subclass3. C: Heatmap analysis of differential lipid components in Subclass3. D: Representative morphological images and C11

BODIPY lipid staining of cells in the in vitro model (Scale bar = 200 μm). E: Cell viability assessed by CCK-8 assay. F: Relative quantification of C11 BODIPY staining mean fluorescence intensity (MFI). G: Relative mRNA expression levels of ERS-related genes in cells. H: Western blot analysis of ERS-related proteins and pyroptosis-related proteins in cells. I: Schematic diagram of the experimental design. J: Serum ALT levels in each group at D3 following 70% PHx. K: Representative Scanning Electron Microscopy (SEM) and Transmission Electron Microscopy (TEM) images of liver tissue at D3 following 70% PHx (Scale bar = 10 μm). L: Representative H&E staining and C11 BODIPY lipid staining images of liver tissue at D3 following 70% PHx (Scale bar = 200 μm). M: Quantification of the percentage of liver injury area following 70% PHx. N: Relative quantification of C11 BODIPY staining. O: Relative mRNA expression levels of ERS-related genes in liver tissue at D3 following 70% PHx. P: Western blot analysis of ERS-related proteins and pyroptosis-related proteins in liver tissue at D3 following 70% PHx. Abbreviations: H, Hypoxia; PA, Palmitic acid; PC, Phosphatidylcholine. Statistical analysis: All quantitative data are presented as Mean ± SD. All quantitative data are presented as Mean ± SD. Statistical significance was determined by one-way ANOVA. Ns: not significant, *$p < 0.05$, **$p < 0.01$, ***$p < 0.001$, and ****$p < 0.0001$.

Figure 4. DR5 is a potential key gene driving pyroptosis following 70% PHx.

A: Volcano plot of DEGs in the first 3 days. B: Cluster dendrogram from Weighted Gene Co-expression Network Analysis (WGCNA). C: Heatmap of module-trait relationships. D: scRNA-seq analysis showing the distribution and clustering of

hepatocyte populations, with red circles highlighting cell populations aggregated after injury. E: Venn diagram showing the screening of key genes from the intersection of RNA-seq DEGs, scRNA-seq DEGs, WGCNA gene modules, and pyroptosis-related gene sets following 70% PHx. F: Ranking of key gene importance screened by machine learning based on DEGs. G: Relative mRNA expression levels of DR5 in the cell model and liver tissue following 70% PHx. H: Western blot analysis of DR5 protein in the cell model and liver tissue following 70% PHx. I: Western blot analysis of pyroptosis-related proteins in the cell model following DR5 knockdown (DR5-KD). J: Schematic diagram of the ALPPS procedure and liver tissue sampling at two stages. K: Western blot analysis of DR5 protein in liver tissue from the first stage-S1 and second stage-S2 of ALPPS in 12 cases. L: Quantification of the Western blot data in K. M: Relative mRNA expression levels of DR5 in liver tissue from S1 and S2 stages of ALPPS in 12 cases. N: Comparison of postoperative serum ALT levels between low and high DR5 expression groups, classified based on DR5 levels after ALPPS-S2. O: Scatter plot of Spearman correlation analysis between relative DR5 mRNA expression in S2 liver tissue and peak postoperative serum ALT levels. Abbreviations: C, Control. All quantitative data are presented as Mean ± SD. Statistical significance was determined by one-way ANOVA (Figure5G).Statistical significance was determined by Student's two-tailed t-test (Figure5L-N). Ns: not significant, $*p < 0.05$, $**p < 0.01$, $***p < 0.001$, and $****p < 0.0001$.

Figure 5. DR5 promotes pyroptosis by impeding FXR nuclear translocation following 70% PHx.

A: Heatmap of proteomics analysis. B: Pseudotime analysis of proteomics data (Subclass1–6). C: KOG functional analysis of Subclass 3 proteins. D: Subcellular localization analysis of Subclass 3 proteins. E: Differential expression of CHPT1 following 70% PHx determined by proteomics. F: Western blot validation of CHPT1 expression in liver tissue following 70% PHx. G: Co-immunoprecipitation (Co-IP) assay detecting the interaction between DR5 and CHPT1. H: Joint functional enrichment analysis of multi-omics (transcriptomics + lipidomics + proteomics) data. I: Western blot detection of DR5 and FXR expression in cytoplasmic and nuclear fractions of the cell model. J: Immunofluorescence images of DR5 and CHPT1 in the cell model (Scale bar = 200 μm). K: Western blot detection of changes in cytoplasmic and nuclear FXR expression following DR5 knockdown (DR5-KD) in the cell model. L: Western blot analysis of pyroptosis-related proteins in the cell model following DR5 knockdown combined with the FXR agonist GW4064. M: Western blot analysis of pyroptosis-related proteins in the cell model following DR5 overexpression (DR5-OE) combined with the FXR agonist GW4064. N: Western blot analysis of pyroptosis-related proteins in the cell model following treatment with the FXR inhibitor Z-GS combined with DR5 knockdown or overexpression. Abbreviations: C, Control; H, Hypoxia; PA, palmitic acid; DR5, death receptor 5; FXR, Farnesoid X receptor; CHPT1, Choline phosphotransferase 1.

Figure 6. The DR5-FXR-CHPT1 axis regulates pyroptosis following 70% PHx.

A: Western blot analysis of CHPT1 in the cell model following DR5 knockdown (DR5-KD) combined with the FXR agonist GW4064. B: Western blot analysis of CHPT1 in the cell model following DR5 overexpression (DR5-OE) combined with the FXR agonist GW4064. C: Western blot analysis of CHPT1 in the cell model following treatment with the FXR inhibitor Z-GS combined with DR5-KD or DR5-OE. D: Sequence analysis of the preferred DNA binding motif of FXR. E: Intersection of GTRD, TCGA, GTEx, and ChIP-Atlas databases predicting potential target genes regulated by FXR as a transcription factor. F: Map of the predicted FXR binding site and modification region in the *Chpt1* promoter, the predicted promoter sequence, and ChIP-qPCR verification of effective regulation of *Chpt1* transcription by FXR activation. G: Correlation between CHPT1 and NR1H4 (FXR) expression in the liver from the GTEx database. H: Immunofluorescence images of DR5, FXR, and CHPT1 in liver tissue from patients with smooth recovery and SFSS following ALPPS (Scale bar = 20 μm). I: Schematic diagram of the experimental design, dosing regimen, and timeline for AAV-DR5, FXR agonist GW4064, and inhibitor Z-GS in the 70% PHx mouse model. J: Serum ALT levels at D3 following 70% PHx in each treatment group. K: Representative HE (Scale bar = 200 μm), SEM (Scale bar = 5 μm), and TEM (Scale bar = 2 μm) images of each group at D3 following 70% PHx. L: Statistical analysis of liver injury area in each group. M: Western blot analysis of CHPT1 expression and pyroptosis-related proteins at D3 following 70% PHx in each group. Abbreviations: GTRD, Gene Transcription Regulation Database; TCGA, The

Cancer Genome Atlas; GTEx, Genotype-Tissue Expression; H&E, Hematoxylin and eosin; SEM, Scanning electron microscopy; TEM, Transmission electron microscopy.

Statistical analysis: Statistical significance was determined by one-way ANOVA (Figure6J and Figure6L). Statistical significance was determined by Student's two-tailed t-test (Figure6F). Data are expressed as mean ± SD. Ns: not significant, *$p < 0.05$, **$p < 0.01$, ***$p < 0.001$, and ****$p < 0.0001$.

Figure 1

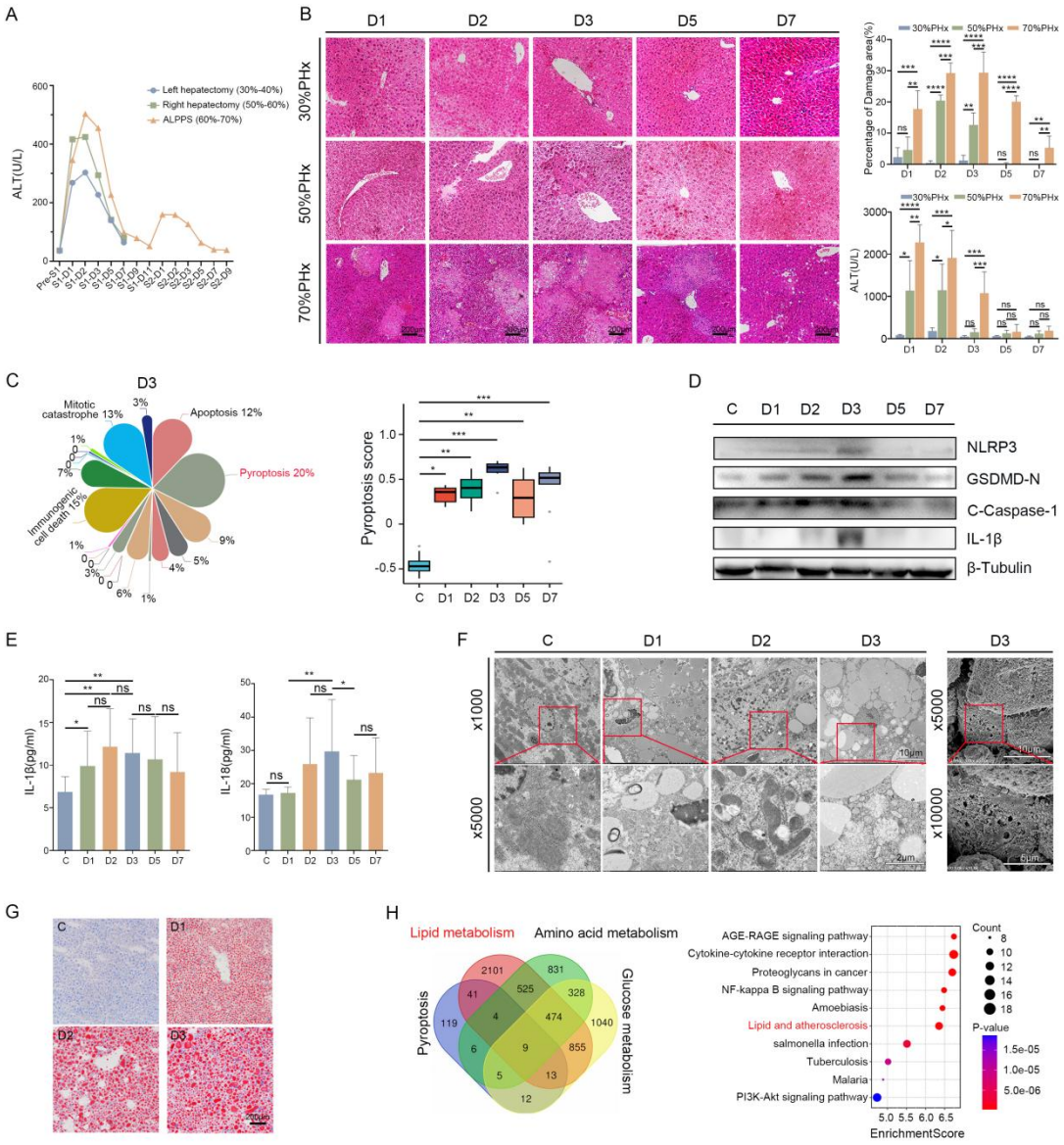

A
ALT(U/L)
Left hepatectomy (30%-40%)
Right hepatectomy (50%-60%)
ALPPS (60%-70%)
B
D1
D2
D3
D5
D7
30%PHx
50%PHx
70%PHx
Percentage of Damage area(%)
ALT(U/L)
C
D3
Mitotic catastrophe 13%
Apoptosis 12%
Pyroptosis 20%
Immunogenic cell death 15%
Pyroptosis score
D
C
NLRP3
GSDMD-N
C-Caspase-1
IL-1β
β-Tubulin
E
IL-1β(pg/ml)
IL-18(pg/ml)
F
x1000
x5000
x10000
G
H
Lipid metabolism
Amino acid metabolism
Glucose metabolism
Pyroptosis
AGE-RAGE signaling pathway
Cytokine-cytokine receptor interaction
Proteoglycans in cancer
NF-kappa B signaling pathway
Amoebiasis
Lipid and atherosclerosis
salmonella infection
Tuberculosis
Malaria
PI3K-Akt signaling pathway
Count
P-value
EnrichmentScore

Figure 2

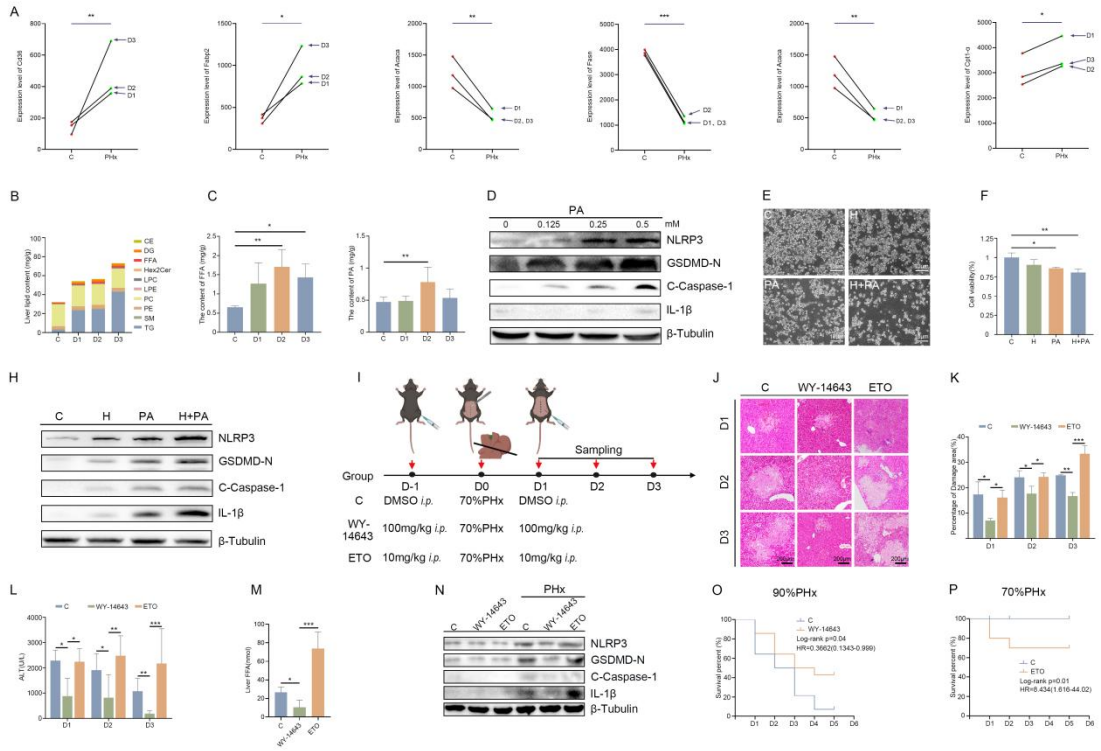

A
B
C
D
PA
NLRP3
GSDMD-N
C-Caspase-1
IL-1β
β-Tubulin
E
F
H
I
Sampling
Group
C
WY-14643
ETO
J
K
L
M
N
PHx
O
90%PHx
P
70%PHx

Figure 3

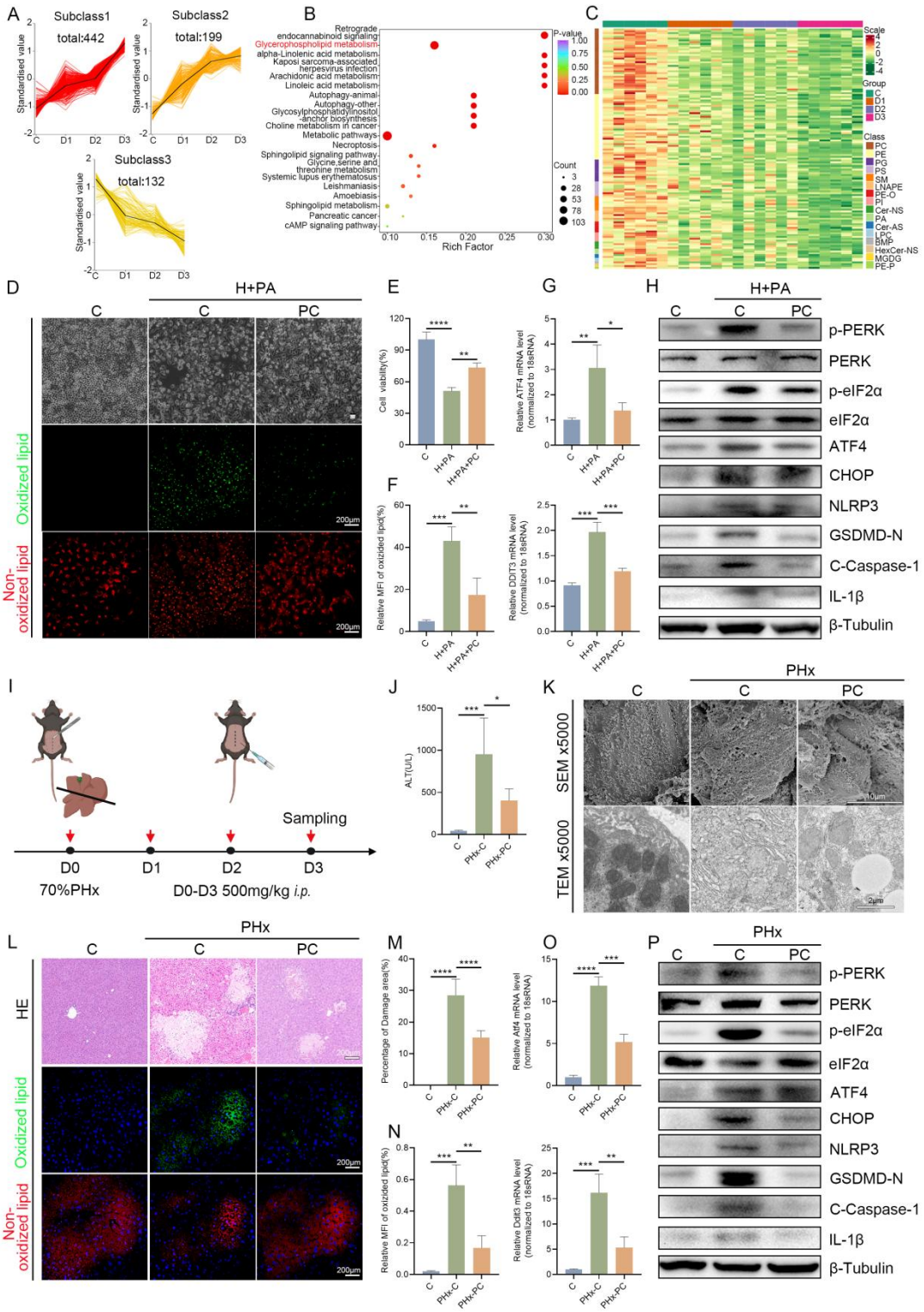

A
Subclass1
total:442
Subclass2
total:199
Subclass3
total:132
Standardised value
C
D1
D2
D3
B
Retrograde endocannabinoid signaling
Glycerophospholipid metabolism
alpha-Linolenic acid metabolism
Kaposi sarcoma-associated herpesvirus infection
Arachidonic acid metabolism
Linoleic acid metabolism
Autophagy-animal
Autophagy-other
Glycosylphosphatidylinositol-anchor biosynthesis
Choline metabolism in cancer
Metabolic pathways
Necroptosis
Sphingolipid signaling pathway
Glycine, serine and threonine metabolism
Systemic lupus erythematosus
Leishmaniasis
Amoebiasis
Sphingolipid metabolism
Pancreatic cancer
cAMP signaling pathway
P-value
Count
Rich Factor
C
Scale
Group
Class
PC
PE
PG
PS
SM
LNAPE
PE-O
PI
Cer-NS
PA
Cer-AS
LPC
BMP
HexCer-NS
MGDG
PE-P
D
H+PA
C
PC
Oxidized lipid
Non-oxidized lipid
200μm
E
Cell viability(%)
H+PA
H+PA+PC
F
Relative MFI of oxidized lipid(%)
G
Relative ATF4 mRNA level (normalized to 18sRNA)
Relative DDIT3 mRNA level (normalized to 18sRNA)
H
p-PERK
PERK
p-eIF2α
eIF2α
ATF4
CHOP
NLRP3
GSDMD-N
C-Caspase-1
IL-1β
β-Tubulin
I
Sampling
D0
D1
D2
D3
70%PHx
D0-D3 500mg/kg i.p.
J
ALT(U/L)
PHx-C
PHx-PC
K
PHx
SEM x5000
TEM x5000
10μm
2μm
L
HE
M
Percentage of Damage area(%)
N
O
Relative Atf4 mRNA level (normalized to 18sRNA)
Relative Ddit3 mRNA level (normalized to 18sRNA)
P

Figure 4

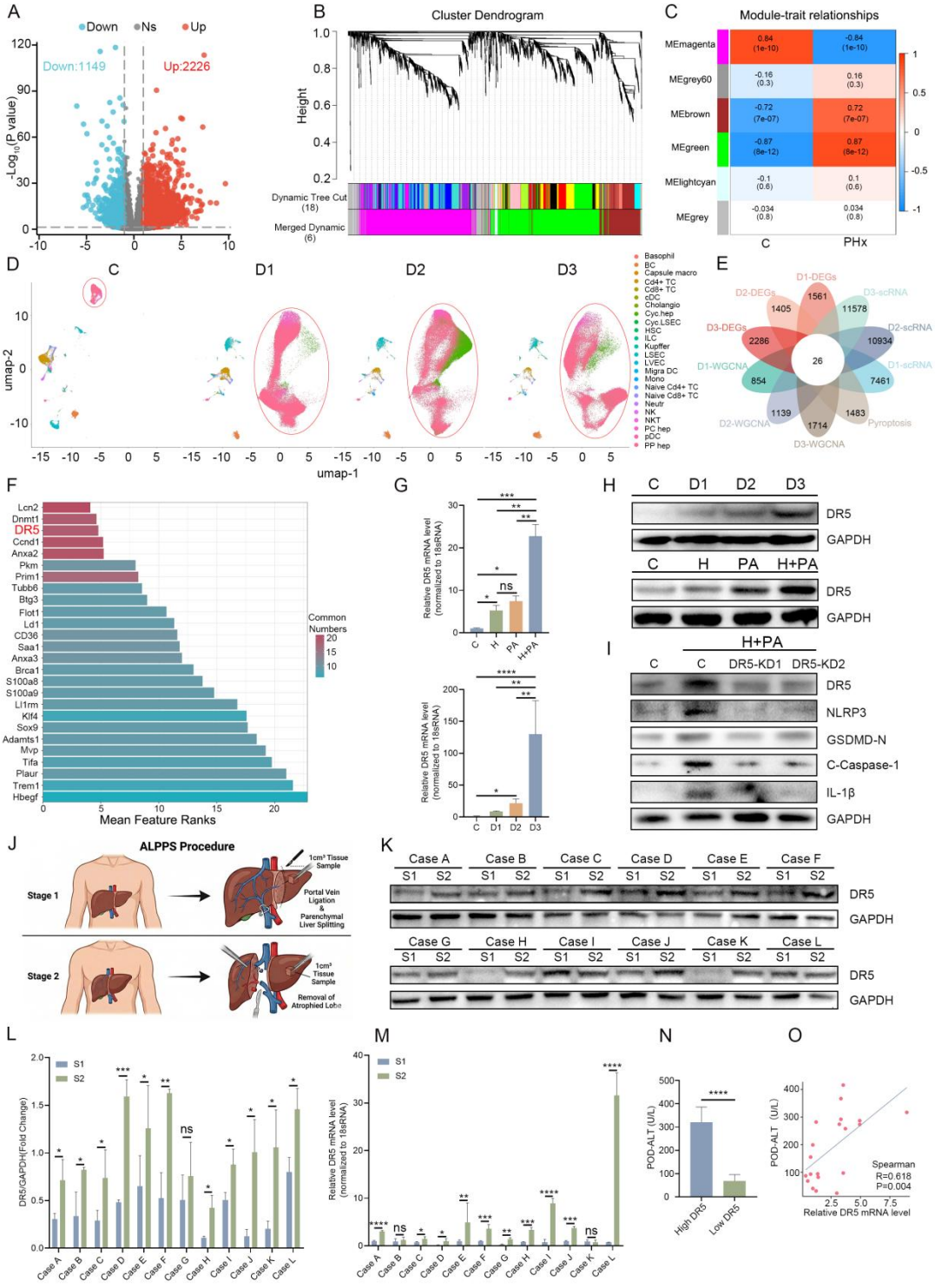

A
Down
Ns
Up
Down:1149
Up:2226
-Log10(P value)
B
Cluster Dendrogram
Height
Dynamic Tree Cut (18)
Merged Dynamic (6)
C
Module-trait relationships
MEmagenta
MEgrey60
MEbrown
MEgreen
MElightcyan
MEgrey
C
PHx
D
C
D1
D2
D3
umap-1
umap-2
Basophil
BC
Capsule macro
Cd4+ TC
Cd8+ TC
cDC
Cholangio
Cyc hep
Cyc LSEC
HSC
ILC
Kupffer
LSEC
LVEC
Migra DC
Mono
Naive Cd4+ TC
Naive Cd8+ TC
Neutr
NK
NKT
PC hep
pDC
PP hep
E
D1-DEGs
D2-DEGs
D3-scRNA
D3-DEGs
D2-scRNA
D1-WGCNA
D1-scRNA
D2-WGCNA
Pyroptosis
D3-WGCNA
F
Lcn2
Dnmt1
DR5
Ccnd1
Anxa2
Pkm
Prim1
Tubb6
Btg3
Flot1
Ld1
CD36
Saa1
Anxa3
Brca1
S100a8
S100a9
Ll1rm
Klf4
Sox9
Adamts1
Mvp
Tifa
Plaur
Trem1
Hbegf
Common Numbers
Mean Feature Ranks
G
Relative DR5 mRNA level (normalized to 18sRNA)
C
H
PA
H+PA
D1
D2
D3
H
DR5
GAPDH
I
H+PA
DR5-KD1
DR5-KD2
NLRP3
GSDMD-N
C-Caspase-1
IL-1β
J
ALPPS Procedure
Stage 1
Stage 2
1cm³ Tissue Sample
Portal Vein Ligation & Parenchymal Liver Splitting
Removal of Atrophied Lobe
K
Case A
Case B
Case C
Case D
Case E
Case F
Case G
Case H
Case I
Case J
Case K
Case L
S1
S2
L
DR5/GAPDH(Fold Change)
M
N
POD-ALT (U/L)
High DR5
Low DR5
O
Spearman
R=0.618
P=0.004
Relative DR5 mRNA level

Figure 5

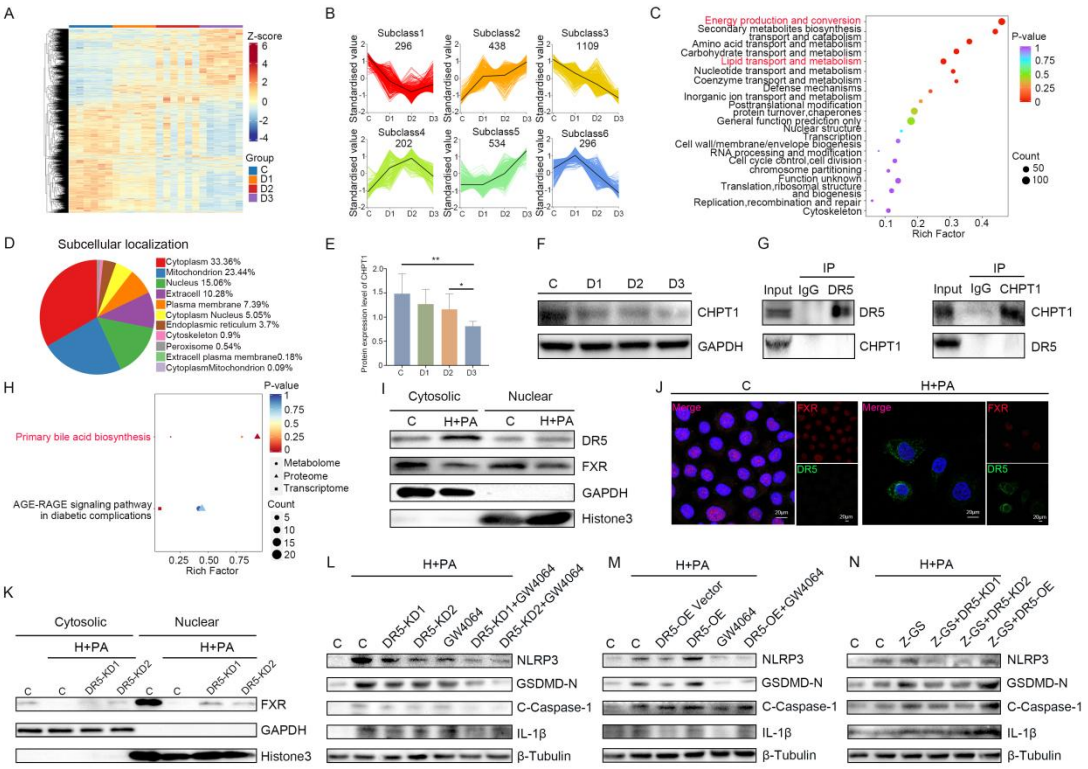

A
Z-score
Group
C
D1
D2
D3
B
Subclass1
296
Subclass2
438
Subclass3
1109
Subclass4
202
Subclass5
534
Subclass6
296
Standardised value
C
Energy production and conversion
Secondary metabolites biosynthesis
transport and catabolism
Amino acid transport and metabolism
Carbohydrate transport and metabolism
Lipid transport and metabolism
Nucleotide transport and metabolism
Coenzyme transport and metabolism
Defense mechanisms
Inorganic ion transport and metabolism
Posttranslational modification
protein turnover,chaperones
General function prediction only
Nuclear structure
Transcription
Cell wall/membrane/envelope biogenesis
RNA processing and modification
Cell cycle control,cell division
chromosome partitioning
Function unknown
Translation,ribosomal structure
and biogenesis
Replication,recombination and repair
Cytoskeleton
P-value
Count
Rich Factor
D
Subcellular localization
Cytoplasm 33.36%
Mitochondrion 23.44%
Nucleus 15.06%
Extracell 10.28%
Plasma membrane 7.39%
Cytoplasm Nucleus 5.05%
Endoplasmic reticulum 3.7%
Cytoskeleton 0.9%
Peroxisome 0.54%
Extracell plasma membrane0.18%
CytoplasmMitochondrion 0.09%
E
Protein expression level of CHPT1
F
CHPT1
GAPDH
G
IP
Input
IgG
DR5
CHPT1
H
Primary bile acid biosynthesis
AGE-RAGE signaling pathway
in diabetic complications
Metabolome
Proteome
Transcriptome
I
Cytosolic
Nuclear
H+PA
DR5
FXR
GAPDH
Histone3
J
C
H+PA
Merge
FXR
DR5
K
L
M
N
DR5-KD1
DR5-KD2
GW4064
DR5-KD1+GW4064
DR5-KD2+GW4064
DR5-OE Vector
DR5-OE
DR5-OE+GW4064
Z-GS
Z-GS+DR5-KD1
Z-GS+DR5-KD2
Z-GS+DR5-OE
NLRP3
GSDMD-N
C-Caspase-1
IL-1β
β-Tubulin

Figure 6

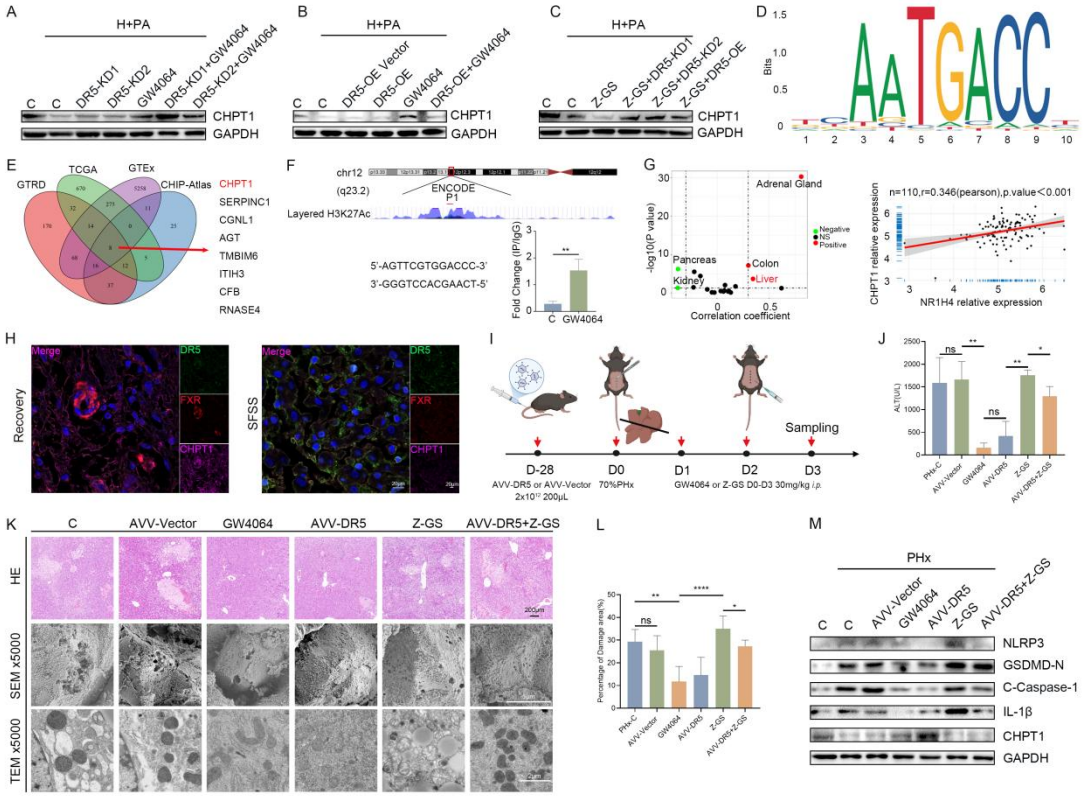
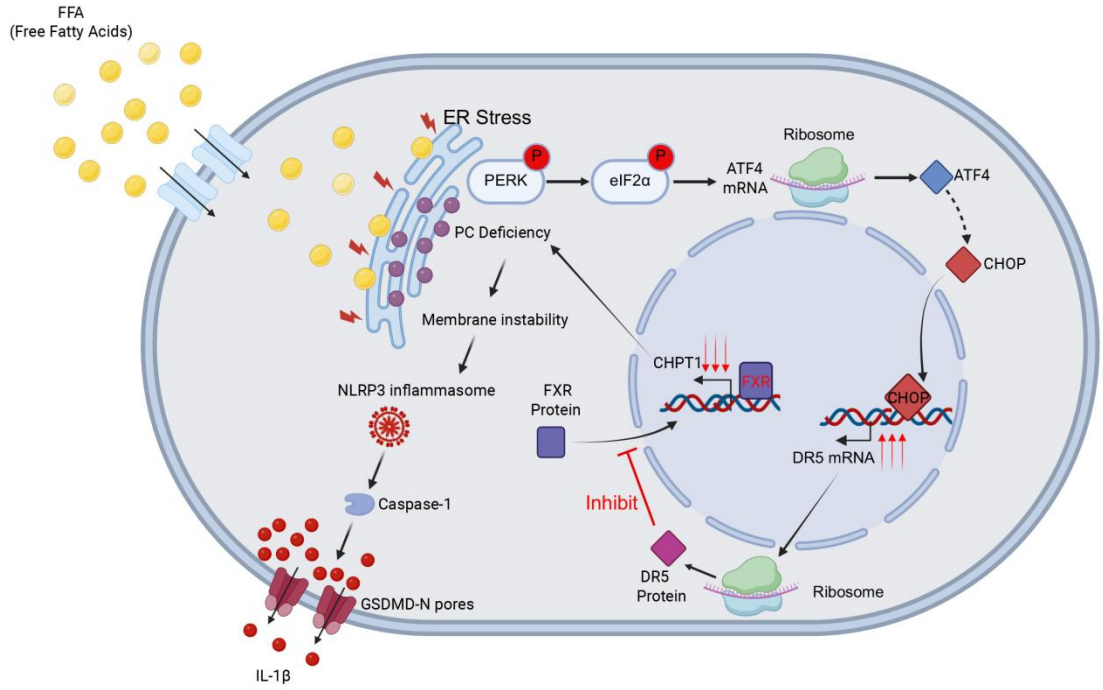

A
H+PA
C C DR5-KD1 DR5-KD2 GW4064 DR5-KD1+GW4064 DR5-KD2+GW4064
CHPT1
GAPDH
B
H+PA
C C DR5-OE-Vector DR5-OE GW4064 DR5-OE+GW4064
CHPT1
GAPDH
C
H+PA
C C Z-GS Z-GS+DR5-KD1 Z-GS+DR5-KD2 Z-GS+DR5-OE
CHPT1
GAPDH
D
Bits
E
GTRD
TCGA
GTEx
CHIP-Atlas
CHPT1
SERPINC1
CGNL1
AGT
TMBIM6
ITIH3
CFB
RNASE4
F
chr12
(q23.2)
ENCODE
P1
Layered H3K27Ac
5'-AGTTCGTGGACCC-3'
3'-GGGTCCACGAACT-5'
Fold Change (IP/IgG)
C GW4064
G
Adrenal Gland
Pancreas
Colon
Liver
Kidney
Negative
NS
Positive
-log10(P value)
Correlation coefficient
n=110,r=0.346(pearson),p.value<0.001
CHPT1 relative expression
NR1H4 relative expression
H
Recovery
SFSS
Merge
DR5
FXR
CHPT1
I
Sampling
D-28
D0
D1
D2
D3
AVV-DR5 or AVV-Vector 2x10^12 200μL
70%PHx
GW4064 or Z-GS D0-D3 30mg/kg i.p.
J
ALT(U/L)
PHx-C AVV-Vector GW4064 AVV-DR5 Z-GS AVV-DR5+Z-GS
K
C
AVV-Vector
GW4064
AVV-DR5
Z-GS
AVV-DR5+Z-GS
HE
SEM x5000
TEM x5000
L
Percentage of Damage area(%)
M
PHx
C C AVV-Vector GW4064 AVV-DR5 Z-GS AVV-DR5+Z-GS
NLRP3
GSDMD-N
C-Caspase-1
IL-1β
CHPT1
GAPDH

Figure 7



Graphical abstract

Following 70% PHx, systemic lipid mobilization leads to massive lipid influx into hepatocytes, triggering ERS. This upregulates death receptor 5 (DR5) expression, which impedes farnesoid X receptor (FXR) nuclear translocation, thereby reducing *Chpt1* (Cholinephosphotransferase 1) transcription and diminishing phosphatidylcholine (PC) synthesis. Consequently, ER stress is progressively exacerbated, ultimately culminating in lethal pyroptosis.

Methords

Clinical specimen collection and data analysis

Clinical data and postoperative liver function parameters (alanine aminotransferase [ALT], aspartate aminotransferase [AST], albumin [ALB], prothrombin time [PT] and international normalized ratio [INR])were retrospectively collected from the Electronic Medical Record System of the Third Affiliated Hospital, Sun Yat-sen University. This study was approved by the Clinical Research Ethics Committee of the Third Affiliated Hospital of Sun Yat-sen University (II2025-316-1). All participants were informed about the study and provided written informed consent before inclusion.

Animals and Mouse models

Wild-type C57BL/6J mice aged 8 weeks were obtained from Jiangsu Gempharmatech Biological Science and Technology Ltd (Nanjing, Jiangsu, China) and bred at the Sun Yat-sen University Laboratory Animals Center. All mice were maintained in a special pathogen-free (SPF) environment with a temperature of 20°C to 25°C, relative humidity of about 50%, and a 12-hour light-dark cycle. All animal procedures were approved by the Institutional Animal Care and Use Committee (IACUC), Sun Yat-Sen University (SYSU-IACUC-2025-001978), and conducted in compliance with National Institutes of Health's Guide for the Care and Use of Laboratory Animals (#JENNIO-IACUC-2024-A062). For the PHx procedure, 8-week-old mice were subjected to liver mass resection[44] (The resection extents were

defined as the left lateral lobe (30%), the left lateral plus half of the median lobe (50%), the left lateral and entire median lobes (70%), and the left lateral, median, and right lobes combined (90%)). Mice were anesthetized with 2% isoflurane (RWD, Shenzhen, China) via induction chamber and maintenance mask. Following a midline incision and exposure of the liver, the bases of corresponding lobes were ligated with silk thread. Once hemostasis was secured, the lobes were excised. The abdomen was sutured, and animals were monitored on a warming pad until fully recovered. Mice were subsequently returned to cages and sacrificed at specific intervals after surgery, with untreated animals utilized as controls.

Immunohistological

Immunohistological staining of liver samples was performed according to the manufacturer's protocol. Briefly, following a sequence of fresh xylene, 100 % ethanol, 100 % ethanol, 95 % ethanol, and 75 % ethanol passing through the cylinder, along with EDTA antigen repair, the slides were then incubated with α-SMA (#19245, CST)、CD45 (ab10558, Abcam)、CD66b (ab300122, Abcam). Subsequently, the sections were stained with Dako secondary antibody (DAKO immunohistochemical kit REAL EnVision) and counterstained with hematoxylin. The mean ± standard deviation (SD) of positive cells per 1000 samples was calculated, followed by counting the labeled cells in 5 fields of view at 200× magnification.

Oil Red O Staining

Frozen liver sections were fixed with 4% paraformaldehyde, pretreated briefly with 60% isopropanol, and stained using a freshly filtered Oil Red O working solution

(Beyotime) for 10-15 minutes at room temperature in the dark. Following differentiation in 60% isopropanol and thorough washing with distilled water, the sections were counterstained with hematoxylin, mounted with an aqueous medium, and examined under a light microscope.

Western blot analysis

Total protein was extracted from the liver tissue and THLE-2 cell line following the manufacturer's protocol. The samples were then separated on 12% sodium dodecyl sulfate-polyacrylamide gels (Bio-Rad, Hercules, CA, USA) and transferred onto polyvinylidene fluoride membranes (Millipore, Bedford, MA, USA). The membranes were blocked with 5% skim milk powder at 25°C for 1 h and incubated overnight at 4°C with the following primary antibodies targeting the following proteins: NLRP3 (ab263899, Abcam)、Gasdermin D (#39754, CST)、IL-1β (ab283818, Abcam)、Cleaved-Caspase-1 (#89332mouse、#4199human, CST)、PERK (#3192, CST)、P-PERK (AP1501, ABclonal)、eIF2α (#5324, CST)、P-eIF2α (AP0692, ABclonal)、ATF4 (DF6008, Affinity)、CHOP (AF6277, Affinity)、DR5 (ab8416, Abcam)、FXR/NR1H4 (#72105, CST)、CHPT1 (A16137, ABclonal) and incubated at room temperature for 1 h with an appropriate secondary antibody conjugated to horseradish peroxidase. The protein signals were visualized with an ECL Western Blotting kit (P10300, NCM, Suzhou, China). ImageJ was used to calculate protein relative expression by plot every gel lane. All protein expression was normalized by loading control (β-Tubulin (#2146, CST), Histone3 (#4499, CST), or GAPDH (#2118, CST)).

Quantitative real-time polymerase chain reaction (qRT-PCR)

Total RNA was isolated using TRIzol (15596026, ThermoFisher), while cDNA synthesis was carried out using the Hiscript III RT Supermix for QPCR (+gDNA Wiper) kit, following the manufacturer's instructions. Subsequently, the cDNA was quantified using a LightCycler 480 high-throughput real-time fluorescent quantitative PCR instrument. The mRNA expression level was normalized to 18s rRNA level. Primers for qRT-PCR were synthesized by Tsingke Company in Wuhan.

Evaluation of liver injury

ALT and AST levels were measured with were measured as indicators of liver injury using an automatic analyzer (Antech Diagnostics). The liver tissues were fixed in 4% paraformaldehyde (PFA), embedded in paraffin, and sectioned to 4-μm thickness, then stained with hematoxylin and eosin (H&E). The damaged area was measured using Image J software. For every sample, five random fields were imaged.

Cell culture and Cell model

Culture flasks were pre-coated with Rat tail collagen type I (C8062, Solarbio) at a concentration of 50 μg/mL dissolved in 20 mM acetic acid, THLE-2 cell line were cultured in THLE-2 Cell Complete Medium (CM-0833, Procell) in a humidified atmosphere of 5% CO2 at 37℃. Hypoxic conditions(H): hypoxic conditions (1% oxygen) for 4 h, and subsequently cultured in normal medium under normoxic conditions for 24 hours. Palmitic acid(PA; Kunchuang Biotechnology) was added to the culture medium according to the corresponding concentration. Hypoxic+Palmitic acid (H+PA) cell model: THLE-2 initially placed in glucose-free DMEM (Gibco)

were cultured under hypoxic conditions (1% oxygen) for 4 h, and subsequently cultured in normal medium supplemented with 0.25 mM PA under normoxic conditions for 24 hours.

Genetic modification

DR5 expression was silenced using a lentiviral CRISPR interference (CRISPRi) system, leveraging the recruitment of the KRAB transcriptional repressor to the target locus. THLE-2 cells were transduced with lentiviral particles generated from an all-in-one vector co-expressing dCas9-KRAB and human DR5-specific sgRNAs (targeting the TSS-proximal promoter region; sgRNA-1: 5'-GACAGGACTATAGCACTCAC-3'; sgRNA-2: 5'-GTGGACACAATCCCTCTGAG-3'). The vector incorporated a Woodchuck Hepatitis Virus Posttranscriptional Regulatory Element (WPRE) to optimize transgene expression. Following transduction, stable cell pools were established through puromycin selection (2 μg/mL for 7 days). The knockdown (KD) efficiency was validated by Western Blotting, confirming a significant and sustained reduction in DR5 protein levels.

Enzyme-linked immunosorbent assay

IL-1β and IL-18 levels in blood were quantified using commercially available ELISA kits (Elabscience, Wuhan), following the manufacturer's protocols.

Animal adeno-associated virus-8 (AAV8) injection and processing

Hepatocyte-specific DR5 knockdown in mice was achieved via tail vein injection of shRNA-carrying adeno-associated virus serotype 8 (mouse-AAV8-shDR5, 1×10^{13}

viral genomes/mL). The shRNA sequence targeting DR5 in mice was GCACAGTCTGTAAGGAAGATA;

AAV viral vectors were generated by PackGene Biotech (Guangzhou, China). After 4 weeks, the PHx model was established with indicated AAV8-treated mice.

Chromatin immunoprecipitation (ChIP) qPCR

The ChIP assays were performed using the ChIP Assay Kit (17-10086,Merck millipore) following the manufacturer's protocol. Briefly, over 1×10^7 THLE-2 cells were cross-linked with 1% formaldehyde at 37°C for 10 minutes, followed by quenching with 1X Glycine Solution at room temperature for 5 minutes. After two washes with PBS containing 1 mM PMSF, the cells were lysed in SDS buffer with 1 mM PMSF on ice (10 minutes). Chromatin was fragmented by sonication (10% intensity, 5-secondpulses) and centrifuged (4°C, 14,000g, 5 minutes). The supernatant was diluted with 2 mL ChIP Dilution Buffer containing 1 mM PMSF. While 10% of each sample was reserved as input, the remainder was immunoprecipitated overnight at 4°C with either NR1H4 antibody or control IgG. After centrifugation (4°C, 1,000g, 1 minute), the pellets were sequentially washed with Low Salt, High Salt, and LiCl Immune Complex Wash Buffers, followed by TE Buffer (4°C, 5 minutes each). Finally, the precipitated DNA was purified for subsequent ChIP-qPCR analysis using *Chpt1* promoter-specific primers (Supplementary Table1), with mouse GAPDH serving as the negative control.

Immunofluorescence staining

Cells were washed with PBS and fixed with 4% paraformaldehyde (PFA) for 30

min at room temperature. After permeabilization with 0.1% Triton X-100 for 10 min, followed by blocking in 10% bovine serum albumin (BSA) in PBS for 30 minutes. Subsequently, the samples were incubated with primary antibodies against DR5 and NR1H4 overnight at 4°C. Following three washes with PBS, the cells were incubated with secondary antibodies, including Alexa Fluor 546-conjugated goat anti-mouse IgG (Invitrogen, Carlsbad, CA, USA) and Alexa Fluor 488-conjugated goat anti-rabbit IgG (Invitrogen, Carlsbad, CA, USA), for 1 h at room temperature in the dark. Nuclei were counterstained with DAPI. Fluorescence images were captured using a laser scanning confocal microscope (Zeiss LSM 880).

FFA concentration detection

The levels of free fatty acids (FFA) in liver tissues were quantified using a commercial Free Fatty Acid Assay Kit (Solarbio, Beijing, China), following the manufacturer's instructions.Briefly, liver tissues samples were weighed and homogenized in the extraction buffer on ice. The homogenates were centrifuged at 8,000 × g for 10 min at 4°C, and the supernatant was collected for analysis. The extraction solution was mixed with the working reagents, and the reaction mixture was incubated at room temperature for 10 min. The absorbance was measured at 550 nm using a microplate reader. The FFA concentration was calculated based on a standard curve and normalized to the tissue weight of the samples.

ScRNA-seq

70%PHx single-cell RNA sequencing

The dataset CNP0002310[28] was sourced from CNGB (https://db.cngb.org/). The

h5ad file was first converted to a Seurat object, preserving the original author's cell type annotations, which were set as the default identity. Rapid quality control was performed, followed by dimensionality reduction and visualization (prioritizing pre-computed Umap embeddings when available) and validation using canonical marker genes. Additional analyses included evaluation of temporal changes in cell type proportions across time points and comprehensive identification of marker genes for all cell types.

90%PHx single-cell RNA sequencing

Preparation of Single-Cell Suspensions

Freshly harvested liver tissues were transferred into Petri dishes containing pre-chilled, RNase-free, calcium- and magnesium-free 1× PBS. The tissues were minced into small fragments (approximately 0.5 mm^2) and washed to remove residual blood, lipids, and other debris. The washed tissue fragments were dissociated using an enzyme cocktail in a 37°C water bath for 30–60 min. Digestion was terminated by adding RPMI 1640 medium (Gibco) supplemented with 2% fetal bovine serum (FBS). The resulting suspension was filtered through a 70-μm cell strainer and centrifuged at 300 × g for 5 min at 4°C. After discarding the supernatant, the cell pellet was resuspended. To remove erythrocytes, cells were treated with 3 mL of Red Blood Cell Lysis Buffer (Solarbio, Beijing, China) on wet ice or at room temperature for 2–10 min. Following lysis, the suspension was centrifuged at 300 × g for 5 min at 4°C. The cell pellet was washed twice by resuspending in 1× PBS containing 0.04% bovine serum albumin (BSA) followed by centrifugation at 300 × g for 3 min at 4°C. Finally,

the cells were resuspended in 1× PBS (0.04% BSA). Cell viability was assessed using AO/PI staining, with a viability threshold of >85% required for downstream processing. Cell counting was performed using a Countess II Automated Cell Counter. When necessary, cell suspensions were optimized using dead cell or debris removal kits (Miltenyi Biotec) to ensure high sample quality.

scRNA-seq Library Construction and Sequencing

Single-cell RNA-seq libraries were constructed using the DNBelab C4 system. Cell capture, cDNA amplification, and library preparation were performed using the DNBelab C Series High-throughput Single-cell RNA Library Preparation Kit V3.0 (MGI Tech) following the manufacturer's protocol, with a target capture of approximately 10,000 cells per sample. The concentration of the libraries was quantified using a Qubit Fluorometer, and fragment integrity was assessed using a Qsep Bio-Fragment Analyzer. The final libraries were sequenced on a DNBSEQ-T7 platform (MGI Tech) using a paired-end 150 bp (PE150) strategy. These services were provided by Guangzhou Angte Biotechnology Co., Ltd. (Guangzhou, China).

RNA-seq

Total RNA was extracted from mouse liver using TRIzol (15596026, ThermoFisher). Bulk RNA-seq libraries were prepared using MGIEasy RNA Library Prep Set (MGI, 1000006384) according to the manufacturer’s instructions and sequenced on an MGISEQ-2000 sequencer at CNGB with paired-end 100 bp.RNA-seq data for gene expression was quantified in an RSEM-based pipeline. DEGs were determined by DESeq2 (v.1.30.1) and defined as having an absolute fold

change of >1.5 and P value of <0.05. Functional annotation was performed with Metascape (v.3.5)84.

Drug

Phosphatidylcholine (PC): Supplementation To enrich cellular membranes with PC, a bovine serum albumin (BSA)-complexed lipid supplementation method was employed as previously described. Briefly, L-α-phosphatidylcholine (P5394, Sigma-Aldrich) was first dissolved in chloroform and dried under a stream of nitrogen gas to form a thin lipid film. The film was resuspended in a 10% (w/v) fatty acid-free BSA solution (prepared in PBS) and incubated at 37°C with continuous vortexing for 1 h until a clear PC-BSA complex was formed. The complex was then sterile-filtered (0.22 μm) and added to the cell culture medium to achieve a final PC concentration of 50 μM[45]. Cells were incubated for 24 h to allow for metabolic incorporation into the membrane bilayers;500 mg/kg for mice in vivo, *i.p.* β-oxidation agonist： WY-14643(HY-16995, MCE; 100mg/kg for mice in vivo, *i.p.*)[46]; β-oxidation inhibitor：Etomoxir(ETO,S8244, Selleck; 10 mg/kg for mice in vivo, *i.p.*)[47]；FXR agonist：GW4064(HY-50108, MCE; 10 μm[48]; 30 mg/kg for mice in vivo, *i.p.*[48,49]); FXR inhibitor: (Z)-Guggulsterone(Z-GS)(HY-110066, MCE; 20 μm; 30 mg/kg for mice in vivo, *i.p.*)[50].

Proteomics Analysis

Sample Preparation and Digestion Tissue samples were ground into powder in liquid nitrogen. The powder was lysed in lysis buffer containing 8 M urea, 1 mM PMSF, and 2 mM EDTA, followed by sonication on ice for 5 min. After

centrifugation at 15,000 × g for 10 min at 4°C, the protein concentration in the supernatant was determined using a BCA assay kit. For digestion, 100 µg of protein was adjusted to a volume of 200 µL with 8 M urea. Samples were reduced with 5 mM dithiothreitol (DTT) for 45 min at 37°C and alkylated with 11 mM iodoacetamide (IAA) for 15 min at room temperature in the dark. The samples were then diluted with 800 µL of 25 mM ammonium bicarbonate and digested with trypsin (Promega, Madison, WI, USA) overnight at 37°C. The digested peptides were acidified to pH 2–3 with 20% trifluoroacetic acid (TFA), desalted using C18 resin (Millipore, Billerica, MA, USA), and quantified using the Pierce™ Quantitative Peptide Assay Kit (Thermo Fisher Scientific).

LC-MS/MS Analysis (Orbitrap Astral) Peptides were separated using a Vanquish Neo UHPLC system (Thermo Fisher Scientific). A trap-and-elute strategy was employed using a PepMap Neo Trap Cartridge (300 µm × 5 mm, 5 µm) and an Easy-Spray™ PepMap™ Neo UHPLC analytical column (150 µm × 15 cm, 2 µm). The mobile phases consisted of 0.1% formic acid in water (A) and 0.1% formic acid in acetonitrile (B). The flow rate was set to 2.5 µL/min with an effective gradient of 6.9 min (total runtime 8 min). Mass spectrometry was performed on an Orbitrap Astral high-resolution mass spectrometer (Thermo Fisher Scientific) in Data-Independent Acquisition (DIA) mode. The instrument operated in positive ion mode with a precursor scan range of 380–980 m/z and a resolution of 240,000 (at 200 m/z). The normalized AGC target was 500% with a maximum injection time (IT) of 5 ms. For MS2 DIA acquisition, 299 scan windows were used with an isolation window

of 2 Th, HCD collision energy of 25%, normalized AGC target of 500%, and maximum IT of 3 ms.

Data Processing Raw MS data were processed using DIA-NN (v1.8.1) with a library-free approach. A spectral library was generated from the mouse proteome database (UniProt UP000000589, 54,910 sequences) using deep learning algorithms. The Match Between Runs (MBR) option was enabled. The False Discovery Rate (FDR) was set to <1% at both the precursor and protein levels for identification and subsequent quantification.

Lipidomics Analysis

Lipid Extraction Tissue samples (20 mg) were ground in liquid nitrogen and extracted with 1 mL of solvent mixture (MTBE:MeOH = 3:1, v/v) containing internal standards. After vortexing for 15 min and adding 200 μL of ultrapure water, the mixture was centrifuged at 12,000 rpm for 10 min. The upper organic layer (200 μL) was collected and dried under vacuum. The residue was reconstituted in 200 μL of acetonitrile/isopropanol (ACN:IPA = 1:1, v/v) for LC-MS/MS analysis.

UPLC-MS/MS Conditions Lipid profiling was performed using an ExionLC AD UPLC system coupled with a QTRAP® 6500+ mass spectrometer (Sciex, Framingham, MA, USA). Separation was achieved on a Thermo Accucore™ C30 column (2.6 μm, 2.1 mm × 100 mm) at 45°C. The mobile phases were (A) acetonitrile/water (60:40, v/v) and (B) acetonitrile/isopropanol (10:90, v/v), both containing 0.1% formic acid and 10 mM ammonium formate. The gradient elution was performed at a flow rate of 0.35 mL/min. The ESI source parameters were set as

follows: source temperature 500°C; ion spray voltage 5500 V (positive) and -4500 V (negative); gas settings GS1 45 psi, GS2 55 psi, and curtain gas 35 psi. Lipid quantification was performed in Multiple Reaction Monitoring (MRM) mode. Data acquisition and processing were conducted using Analyst 1.6.3 software and the MetWare database (MetWare Biotechnology Co., Ltd., Wuhan, China).

Nuclear and Cytoplasmic Fractionation

Nuclear and cytoplasmic proteins were extracted using the Nuclear and Cytoplasmic Protein Extraction Kit (Cat# P0028, Beyotime Biotechnology, Shanghai, China) according to the manufacturer's protocol. Briefly, cells were harvested, washed with ice-cold PBS, and resuspended in Cytoplasmic Extraction Reagent A supplemented with 1 mM PMSF. After incubation on ice for 15 min, Cytoplasmic Extraction Reagent B was added, and the mixture was vigorously vortexed for 5 s and incubated on ice for 1 min. The samples were then centrifuged at 12,000 × g for 5 min at 4°C. The resulting supernatant (cytoplasmic fraction) was collected. The remaining pellet was resuspended in Nuclear Extraction Reagent containing PMSF and vortexed intermittently for 30 min on ice. Following centrifugation at 16,000 × g for 10 min at 4°C, the supernatant (nuclear fraction) was collected. Protein concentrations were determined using a BCA Protein Assay Kit.

Co-Immunoprecipitation (Co-IP)

Cell lysates were prepared using IP lysis buffer and incubated with specific antibodies against DR5/CHPT1 or control IgG overnight at 4°C. The immune complexes were captured using Protein A/G Magnetic Beads (Elabscience, Wuhan,

China) for 2 h. After extensive washing with a magnetic separator, the bound proteins were eluted by boiling in SDS sample buffer and subjected to Western blot analysis to detect the interaction with CHPT1/DR5.

Cell Counting Kit-8 assay (CCK-8)

Adherent primary hepatocytes were plated in 96-well plates, and each group was spread with 3-5 holes. Each hole was filled with 200 μL medium or configured drugs. During the detection, the culture medium was replaced, 10 μL CCK-8 (KGA317-2, KeyGEN) and 100μL culture medium (Gibco) were added to each well, and incubated at 37℃ for 2 h. Finally, the absorbance at 450 nm was measured using a microplate reader.

Machine learning models

We implemented 15 distinct machine learning algorithms using the R programming language. The algorithms included Neural Network (Multilayer Perceptron [NN-MLP]), Lasso Regression, Extreme Gradient Boosting (XGBoost), Elastic Net Regression (ENR), Support Vector Machine (SVM), Gradient Boosting Machine (GBM), Ridge Regression (RR), K-Nearest Neighbors (KNN), Linear Discriminant Analysis (LDA), Quadratic Discriminant Analysis (QDA), Logistic Regression (LR), Decision Tree (DT), Random Forest (RF), Naive Bayes, and Stepwise Logistic Regression based on AIC (Stepwise-AIC).To optimize performance, we utilized the caret package for hyperparameter tuning. By integrating custom parameter grids, Lasso-based feature selection, and cross-validation strategies, we constructed and evaluated a total of 207 specific model combinations(The machine

learning models were trained using our transcriptomic dataset (Training Set). Subsequently, the predictive performance of the optimal models was rigorously tested using four independent external validation cohorts, including GSE151309(data2), GSE20426(data3), GSE181476 (data4), and CNP0002310 (data5).

Multiplex immunohistochemical (mIHC) staining

Multiplex Immunofluorescence Staining Multiplex immunofluorescence (mIF) staining was performed on formalin-fixed, paraffin-embedded liver sections using a 4-color Multiplex Fluorescent Immunohistochemistry Kit (Servicebio, Wuhan, China). Following deparaffinization and microwave-based antigen retrieval in citrate or EDTA buffer, endogenous peroxidase was blocked, and sections were incubated with primary antibodies overnight at 4°C. A sequential staining protocol was employed based on Tyramide Signal Amplification (TSA) technology, where each cycle consisted of HRP-conjugated secondary antibody incubation, TSA-fluorophore reaction, and heat-induced antibody stripping. Target proteins were grouped into distinct panels on serial sections, utilizing antibodies against CD206 (#24595, CST), iNOS (ab3523, Abcam), F4/80 (ab300421, Abcam), CD3 (ab135327, Abcam), CD19 (ab245235, Abcam), NCR-1 (ab233558, Abcam), DR5 (ab8416, Abcam, Cambridge, UK) and NR1H4 (#72105, CST, Danvers, MA, USA), as well as CHPT1 (A16137, ABclonal). Finally, nuclei were counterstained with DAPI, and images were acquired using

Transmission electron microscopy(TEM)

The anesthetized mice were perfused with 0.9% saline, and 1 mm3 liver tissue

blocks were obtained. Next, the fresh tissue blocks were immersed into fixative for TEM (Servicebio) at 4℃ for 4 h. They were then treated with 1% OsO4 in 0.1 mol/L PBS for 2 h at room temperature, followed by a dehydration process with gradient alcohol. Subsequently, the sections were embedded and underwent baking in an oven at 60℃ for 48 h and cut into ultrathin sections (60 nm) using an ultramicrotome. Finally, the ultrastructure of the tight junctions of the liver was observed using a transmission electron microscope (HITACHI) as described previously.

Scanning Electron Microscopy (SEM)

Liver tissues were cut into 5 mm^2 blocks, washed with PBS, and fixed in EM fixative for 2 h at room temperature (stored at 4°C).Samples were washed in 0.1 M PB (pH 7.4) and post-fixed with 1% OsO_4 for 1–2 h in the dark. Then, tissues were dehydrated in a graded ethanol series (30% to 100%) and substituted with isoamyl acetate. Samples were critical-point dried, mounted on conductive carbon tape, and sputter-coated with gold for 30 s prior to SEM (HITACHI) imaging.

Statistical analyses

All experiments were performed at least three times. All data are presented as means±SD. Depending on the data, Student’s t test or one-way ANOVA. Correlation between two groups was measured by the Pearson correlation analysis. Kaplan-Meier method and log-rank test were utilized for survival analyses.Statistical significance was considered at a two-sided p value<0.05. The level of significance is indicated as *p <0.05, **p<0.01, and ***p <0.001. All statistical analyses were performedusing the GraphPad Prism (Version 8.0.1), or statistical package R.

Supplementary Files

This is a list of supplementary files associated with this preprint. Click to download.

- supplementaryinformation.docx